J. Fluid Mech. (2009), *vol.* 619, *pp.* 45–78.
doi:10.1017/S0022112008004382 Printed in the United Kingdom

Water entry of small hydrophobic spheres

JEFFREY M. ARISTOFF
AND JOHN W. M. BUSH†

Department of Mathematics, Massachusetts Institute of Technology,
Cambridge, MA 02139, USA

(Received 4 March 2008 and in revised form 16 September 2008)

We present the results of a combined experimental and theoretical investigation of the normal impact of hydrophobic spheres on a water surface. Particular attention is given to characterizing the shape of the resulting air cavity in the low Bond number limit, where cavity collapse is driven principally by surface tension rather than gravity. A parameter study reveals the dependence of the cavity structure on the governing dimensionless groups. A theoretical description based on the solution to the Rayleigh–Besant problem is developed to describe the evolution of the cavity shape and yields an analytical solution for the pinch-off time in the zero Bond number limit. The sphere's depth at cavity pinch-off is also computed in the low Weber number, quasi-static limit. Theoretical predictions compare favourably with our experimental observations in the low Bond number regime, and also yield new insight into the high Bond number regime considered by previous investigators. Discrepancies are rationalized in terms of the assumed form of the velocity field and neglect of the longitudinal component of curvature, which together preclude an accurate description of the cavity for depths less than the capillary length. Finally, we present a theoretical model for the evolution of the splash curtain formed at high Weber number and couple it with the underlying cavity dynamics.

1. Introduction

Worthington & Cole (1897, 1900) used single-spark photography to examine the air cavity formed by the vertical entry of spheres into water and so initiated the scientific investigation of solid–liquid impacts. Subsequent studies by Mallock (1918) and Bell (1924) provided some qualitative explanation for the observed cavity shapes and sphere trajectories. The advent of high-speed cine-photography allowed for quantitative measurements, the first series of which explored the influence of the atmospheric pressure on the water entry of missiles (Gilbarg & Anderson 1948; Richardson 1948). Additional investigations of the water-entry cavity and surrounding flow field were performed by Birkhoff & Caywood (1949), Birkhoff & Isaacs (1951), Birkhoff & Zarantonello (1957) and Abelson (1970), but the most extensive ones were conducted by May (1951, 1952, 1975) with a view to naval ordinance applications.

Military applications also prompted studies of the impact forces generated during landing and sliding of planes on liquid surfaces (von Karman 1929; Wagner 1932). During World War II, Barnes Wallis developed a spinning cylindrical bomb that could skip along the water surface towards its target, thereby bypassing underwater nets (Whalley 2002). Commonly known as Dam Busters, these bombs were successfully

† Email address for correspondence: bush@math.mit.edu

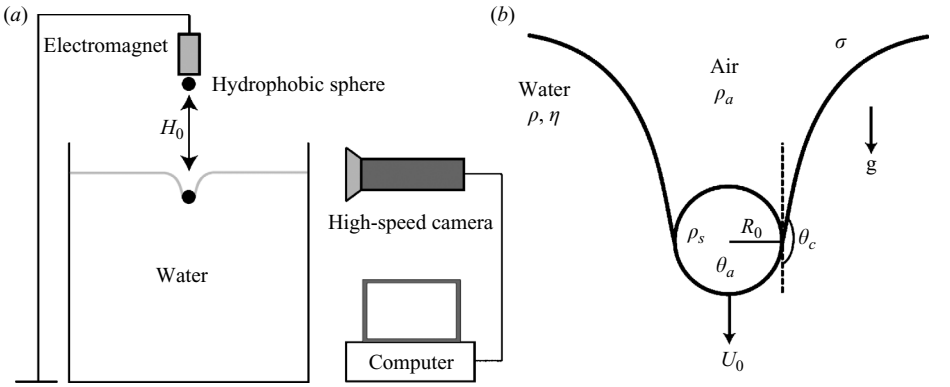

FIGURE 1. Schematic of (*a*) the experimental apparatus and (*b*) the impact parameters. The advancing contact angle is θ_a, and the cavity cone angle is θ_c.

used to breach the Moehne and Eder dams. Drag reduction on underwater projectiles via supercavitation, a process that surrounds the projectile with a sustained vapour cavity, is currently being explored and holds promise in air-to-sea weaponry (Ashley 2001).

Impacts also arise in both geophysical and astrophysical settings. High-energy meteorite impacts may liquify both the impactor and the target, leading to features (e.g. crater formation, secondary meteorites, impact jetting) reminiscent of high Reynolds number solid–liquid impacts. For a review of cratering mechanics associated with meteorite impacts, see for example Melosh (1980) and Melosh & Ivanov (1999). Fluidlike flow of granular materials has been demonstrated in the laboratory by dropping metal spheres into loosely packed sand. Granular impacts possess several similarities to their fluid counterparts, including void collapse and jet formation (Thoroddsen & Shen 2001; Lohse *et al.* 2004*a*), and offer insight into the dynamics of quicksand (Lohse *et al.* 2004*b*).

Biological applications of solid–liquid impacts include locomotion at the air–water interface (Bush & Hu 2006). Large water walkers such as basilisk lizards and some shore birds rely on inertial forces generated by the impact of their driving leg for weight support. Glasheen & McMahon (1996*a*) demonstrated that a basilisk lizard supports itself on water by slapping the surface and stroking its foot downwards to create an expanding air cavity. The lizard then retracts its foot before the cavity collapses in order to minimize drag. By studying the vertical water entry of disks, Glasheen & McMahon (1996*b*) found an empirical relationship for the time of cavity closure. Small water walkers such as insects and spiders rely on surface tension for both weight support and propulsion, and their rough hairy surface renders them water-repellent (Bush, Prakash & Hu 2008). The impact of small hydrophobic bodies on a water surface thus has implications for the locomotion of small water walkers. Moreover, the dynamics of small-scale cavity closure is relevant to a number of insects, including predacious diving beetles and the ichneumon wasp, which violently penetrate the free surface in search of prey (Ward 1992).

Consider a solid sphere with density ρ_s and radius R_0 impacting a horizontal water surface with vertical speed U_0 as depicted in figure 1(*b*). The impact may be characterized by five dimensionless groups: Weber number $W = \rho U_0^2 R_0/\sigma$, Bond number $B = \rho g R_0^2/\sigma$, Reynolds number $Re = \rho U_0 R_0/\eta$, solid–liquid density ratio $D = \rho_s/\rho$ and the air–liquid density ratio $\tilde{D} = \rho_a/\rho$, where σ is the surface tension, η

the dynamic viscosity of the liquid, ρ the liquid density, ρ_a the air density and g the gravitational acceleration. We note that W describes the relative magnitude of fluid inertia to capillary forces, while B describes the relative magnitude of gravitational to capillary forces. High B ($B \gg 1$) impacts are typically classified by their Froude number $F = U_0^2/gR_0 = W/B$ and may be divided into distinct dynamical regimes based upon the type of cavity collapse. One may also introduce a sixth parameter θ_a, the advancing contact angle, to characterize the surface properties of the solid. For air–water entry, this parameter has been shown to determine the threshold impact speed for air entrainment and hence cavity formation. Duez *et al.* (2007) demonstrate that for $W \gtrsim 10^3$, hydrophilic spheres require a larger impact velocity to produce a cavity than do their hydrophobic counterparts. We shall observe a similar trend at lower W. Finally, for high-speed impacts, cavitation bubbles may form if the cavitation number $Q = (p - p_v)/(1/2\,\rho U_0^2) < 1$, where p is the local pressure and p_v the water vapour pressure. In our study, $Q \gg 1$, and so the creation of cavitation bubbles in the liquid need not be considered.

The initial stage of water entry has been considered by Korobkin & Pukhnachov (1988), Howison, Ockendon & Wilson (1991) and Oliver (2007). Thoroddsen *et al.* (2004) observed that for $Re > 2 \cdot 10^4$, a nearly horizontal sheet may emerge from the edge of an impacting sphere within 100 μs of impact, accounting for an estimated 90 % of the total kinetic energy transferred from the sphere to the liquid in this initial stage. Although our camera is not capable of recording events at this time scale, the values of Re in our study are well below this critical value.

The growth and pinch-off of cavities at high B were investigated by Gilbarg & Anderson (1948), Birkhoff & Isaacs (1951), May (1952), Glasheen & McMahon (1996*b*) and Gaudet (1998) for various F ranges. Gekle *et al.* (2008) investigated the cavity formed behind a vertical cylinder pulled at a constant speed through a water surface. They observed two asymptotic F scalings for the dimensionless pinch-off depth, one for $F \ll 10$, the other for $F \gg 10$, separated by discrete jumps. The discontinuous behaviour was rationalized in terms of the capillary waves initiated when the top of the cylinder passed the water surface; numerical simulations confirmed this rationale. In § 2, we will observe analogous behaviour for low B impacts, the rationale for which will be provided in § 6.1.

Lee, Longoria & Wilson (1997) investigated the cavity formed by the vertical water entry of arbitrarily shaped projectiles at high B and $F \geqslant 150$. A theoretical model was developed by assuming that the kinetic energy lost by the projectile equals that fed into a horizontal fluid section. Their model predicted that pinch-off would occur near the surface at a time independent of F but dependent on $\tilde{D}$. Their model was found to be in good agreement with the experiments of Gilbarg & Anderson (1948), who investigated the influence of the air density on the cavity evolution. Bergmann *et al.* (2006) considered the pinch-off of a cylindrical cavity created when a disk is pulled through a water surface at $B \approx 125$ and provided evidence against the self-similarity of cavity collapse. Grumstrup, Keller & Belmonte (2007) elucidated the volume oscillations that may be observed on the bubble attached to the body following pinch-off.

Duclaux *et al.* (2007) investigated the cavity formed by the vertical water entry of both spheres and cylinders at high B and $1 \leqslant F \leqslant 80$. They developed a theoretical model for the cavity evolution based on an extension of the method used to solve the Rayleigh–Besant problem: the collapse of a spherical cavity in a fluid of infinite extent (Besant 1859; Rayleigh 1917). By considering a purely radial flow that is initiated by the passing of the projectile, Duclaux *et al.* (2007) derived an approximate analytical

expression for the evolution of the cavity and thus rationalized the empirical scalings found by Glasheen & McMahon (1996*b*) and Lohse *et al.* (2004*a*). A similar approach will be taken in our theoretical developments.

Studies of low B solid–liquid impacts have been primarily limited to low W. Vella, Lee & Kim (2006*a*, *b*), for example, consider the forces acting on a low W impactor, and show that a quasi-static description of the resulting cavity is sufficient in order to describe the contact line motion. Further insight into the maximum weight supportable by an interface is provided by Vella & Metcalfe (2007), who study the impact of a line mass in which the liquid inertia is entirely negligible. Lee & Kim (2008) investigated a striking phenomenon in which a small superhydrophobic sphere may bounce off a water surface, even for $D > 1$, and propose a rebound criterion that is in good agreement with the experiment. For a detailed study of the forces acting on and between floating bodies, see for example Mansfield, Sepangi & Eastwood (1997) and Kralchevsky & Denkov (2001).

In the present study, we restrict our attention to dense hydrophobic spheres that sink even at low W and focus on the shape of the resulting air cavity. One expects a small sphere ($B \ll 1$) impacting at sufficiently high speed to generate a slender cavity with characteristic radius R_0. If the cavity dynamics are dominated by surface tension, one then might further expect its breakup to be governed by a Rayleigh–Plateau-like instability, which will result in its pinching off into a chain of bubbles of characteristic volume $\Omega \approx 13\pi R_0^3$ after a time $t_{pinch} \approx 1.2\sqrt{\rho R_0^3/\sigma}$ (Chandrasekhar 1961). We shall demonstrate that this physical picture is incomplete on two grounds. First, even at low B, gravity becomes important in the cavity pinch-off at depths greater than l_c^2/R_0, where $l_c = \sqrt{\sigma/(\rho g)} \approx 0.27\,\text{cm}$ is the capillary length. Second, the cavity expands radially following impact, and its W-dependent shape necessarily influences pinch-off.

We extend the work of Duclaux *et al.* (2007) by including the effects of surface tension and aerodynamic pressure on the cavity evolution. In § 2 we describe our experimental technique and the variety of cavity types observed in our study. The sphere's trajectory is discussed in § 3, and a theoretical model for the cavity dynamics is developed in § 4. In § 5 we examine impacts for which inertia can be neglected, and in § 6 we consider impacts for which inertia becomes important. Particular attention is given to rationalizing the pinch-off time and depth of the cavity and the dependence of the cavity shape on the governing dimensionless groups. A theoretical model for the evolution of the splash curtain is presented in § 7, and in § 8 we summarize the value and limitations of our models.

2. Experimental study

Figure 1(*a*) is a schematic of our experimental apparatus. A hydrophobic steel sphere is held by an electromagnet at a height H_0 above a water tank 40 cm long, 20 cm wide and 25 cm deep. The sphere is released from rest and falls towards the water, reaching it with a speed $U_0 \approx \sqrt{2gH_0}$. The impact sequence is recorded at 2000 to 5000 frames per second using a Vision Research Phantom V5.1 high-speed video camera. Midas 2.1 imaging software is used to analyse the images and measure the precise impact speed.

A hydrophobic spray coating, WX2100 by Cytonix Corp., was used to prepare the spheres. Two coats were applied, the second a day after the first. The coatings did not appreciably affect the sphere density $\rho_s = 7.7 \pm 0.1\,\text{g cm}^{-3}$ or radii $0.6\ \text{mm} < R_0 < 9\,\text{mm}$ but did increase the advancing contact angle from $\theta_a = 90 \pm 5^\circ$ to $\theta_a = 120 \pm 5^\circ$, values measured using the sessile drop method (Hiemenz

Dimensionless group	Symbol	Definition	Order of magnitude
Weber number	W	$\frac{\rho U_0^2 R_0}{\sigma}$	$10^{-1} - 10^3$
Bond number	B	$\frac{\rho g R_0^2}{\sigma}$	$10^{-2} - 10$
Reynolds number	Re	$\frac{\rho U_0 R_0}{\eta}$	$10^2 - 10^4$
Density ratio (solid-liquid)	D	$\frac{\rho_s}{\rho}$	10
Density ratio (air-liquid)	$\tilde{D}$	$\frac{\rho_a}{\rho}$	10^{-3}
Advancing contact angle	θ_a	θ_a	$115^\circ - 125^\circ$
Froude number	F	$\frac{U_0^2}{g R_0}$	$10^{-1} - 10^5$
Cavitation number	Q	$\frac{p - p_v}{1/2\,\rho U_0^2}$	$10 - 10^4$

TABLE 1. Relevant dimensionless groups and their characteristic values in our experimental study. Sphere radii were between $R_0 = 0.6$ mm and 9 mm and impact velocities between $U_0 = 10$ cm s^{-1} and 1 000 cm s^{-1}.

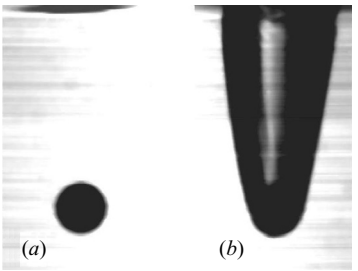

FIGURE 2. The influence of surface coating on a water-entry cavity at low B. (*a*) Polished steel sphere. (*b*) Steel sphere with hydrophobic coating. Both photographs were taken 3.4 ms after impact. The level of the undisturbed free-surface corresponds to the top of each image; $B = 0.2$; $W = 170$; $D = 7.7$.

& Rajagopalan 1997). Surface roughness measurements were made using a Tencor P-10 surface profilometer. The root mean square displacements of the roughness profiles were computed for the polished spheres (0.0318 μm ± 5 %) and coated spheres (1.824 μm ± 0.01 %) and indicate a 50-fold increase due to the surface treatment. The experiments were performed at atmospheric pressure and the temperature of the water remained between 21° and 23°C. The relevant dimensionless groups and their range in our experimental study are listed in table 1.

An important foundation of the present study is the observation reported by Duez *et al.* (2007) that hydrophobicity promotes air entrainment by impacting spheres. In figure 2, two steel spheres, identical in every aspect but their surface coatings, are shown 3.4 ms after impact. The polished sphere (figure 2*a*) entrains relatively little air; the sphere with a hydrophobic coating (figure 2*b*) generates a substantial axisymmetric air cavity with a well-defined shape. Coated, hydrophobic bodies were examined in all subsequent experiments.

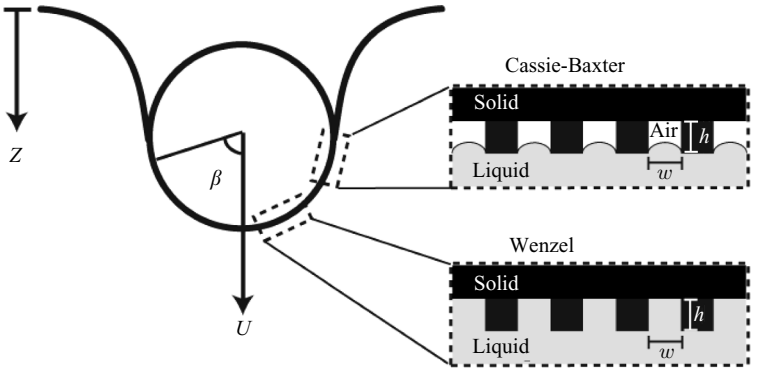

FIGURE 3. Idealized model of surface roughness illustrating the possibility of two wetting states. Pockets of air are trapped between the solid and water in the Cassie-Baxter state, while in the Wenzel state, the solid surface is entirely wetted. The roughness is exposed to an intrusion pressure $\rho U^2 \cos^2\beta + \rho g Z$.

The presence or absence of an air film trapped between the water and the impacting sphere determines whether the surface is in a Cassie-Baxter or Wenzel state, respectively, and may be rationalized by the simple model illustrated in figure 3. Let the roughness be represented by a periodic array of posts with separation w and height h, and let the sphere centre have depth Z and speed U. Pockets of air will remain trapped between the posts if the characteristic curvature pressure ($\sigma h/w^2$ if $h < w$ and σ/w if $h \geqslant w$) exceeds the impregnation pressure ($\rho U^2 \cos^2\beta + \rho g Z$), which has both dynamic and hydrostatic components (De Gennes, Brochard-Wyart & Quere 2004). Estimates of the characteristic post spacing $w \approx 20\,\mu$m and post height $h \approx 1\,\mu$m were deduced from the profilometer measurements. Hydrostatic pressure will cause impregnation beyond a wetting depth $Z_w \sim \sigma h/(\rho g w^2) \sim 2$ cm. Likewise, dynamic pressure will cause impregnation for speeds exceeding a wetting speed $U_w \sim \sqrt{\sigma h/(\rho w^2 \cos^2\beta)} \sim 40$ cm s^{-1}. Note that the latter condition depends on β; so the sphere could have a mixed state, Wenzel at the nose and Cassie-Baxter at the equator (figure 3).

For high-speed impacts, it is difficult to observe the detailed contact line dynamics; in lieu of a detailed examination thereof, we introduce the parameter, θ_c, defined as the angle that the cavity makes as it leaves the sphere with respect to the vertical tangent (see figure 1*b*). We call this the 'cone angle' and observe that, after an initial adjustment phase, it is approximately constant as a function of depth and body speed for a given surface material. Thus, it can be measured by a single experiment. We do not attempt to characterize the relation between θ_c and the advancing contact angle θ_a in this study but instead simply report that $160^\circ < \theta_c < 170^\circ$ for the impacting spheres studied.

For the impact of hydrophobic spheres at low B, we have observed four distinct cavity types that we will describe in turn. A typical low W impact of a hydrophobic sphere is shown in figure 4. The sphere sinks and is completely immersed in water after ~ 0.01 s. Both the vertical and radial extents of the cavity are of the order of the capillary length. The measured contact angle remains nearly constant as the contact line slips around the sphere, an observation consistent with those of Ablett (1923) for a hydrophobic solid at an air–water interface and Vella *et al.* (2006*b*) for the sinking of a dense horizontal cylinder. Cavity collapse occurs when the contact line approaches the apex of the sphere (figure 4*h*), at a depth of approximately l_c.

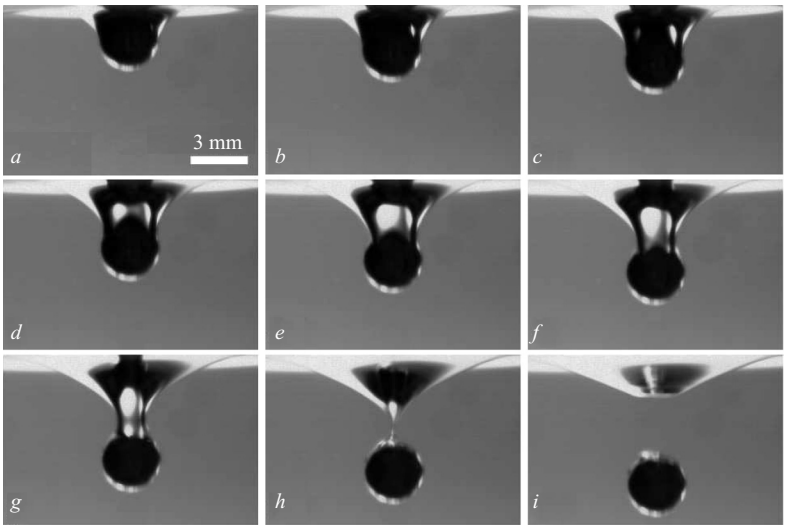

FIGURE 4. Quasi-static impact cavity. Video sequence of the water entry of a hydrophobic steel sphere at low B ($R_0 = 0.14$ cm, $\rho_s = 7.7$ g cm^{-3}, $U_0 = 30$ cm s^{-1}). The time between successive images is 1.1 ms; $W = 1.9$; $B = 0.27$.

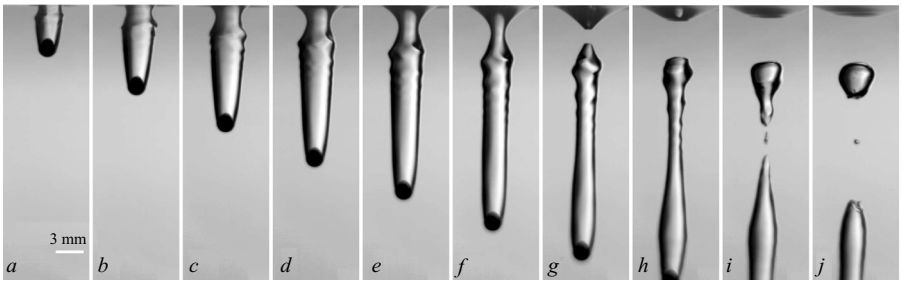

FIGURE 5. Shallow seal impact cavity. Video sequence of the water entry of a hydrophobic steel sphere at low B ($R_0 = 0.10$ cm, $\rho_s = 7.7$ g cm^{-3}, $U_0 = 230$ cm s^{-1}). The time between successive images is 1.9 ms; $W = 72$; $B = 0.14$.

Air entrainment is minimal. Only a tiny bubble remains attached to the sphere after pinch-off (figure 4*i*). We also observe what appears to be an air layer surrounding the sphere, as indicated by the sphere's halo in figure 4. In this regime, we expect the dominant balance to be between gravity and surface tension as for a static meniscus. We thus define this regime as 'quasi-static': at the leading order, the cavity should take the shape of a static meniscus adjoining the sphere at the advancing contact angle. The maximum vertical extent of a two-dimensional static meniscus is of the order of the capillary length (Mansfield *et al.* 1997). The analogous axisymmetric, quasi-static impact is considered in § 5, where we demonstrate that the sphere's depth at cavity pinch-off can be significantly less than the capillary length.

As W increases, the impact generates a substantial air cavity and ripples that propagate down the resulting free surface at speeds less than that of the sphere (figure 5). In Appendix B, we will show that these ripples correspond roughly to the capillary waves expected to arise on a cylindrical cavity. Following an initial adjustment phase, the contact line appears fixed near the level of the sphere's equator, from which the interface is swept upwards, resulting in a highly sloped cavity wall.

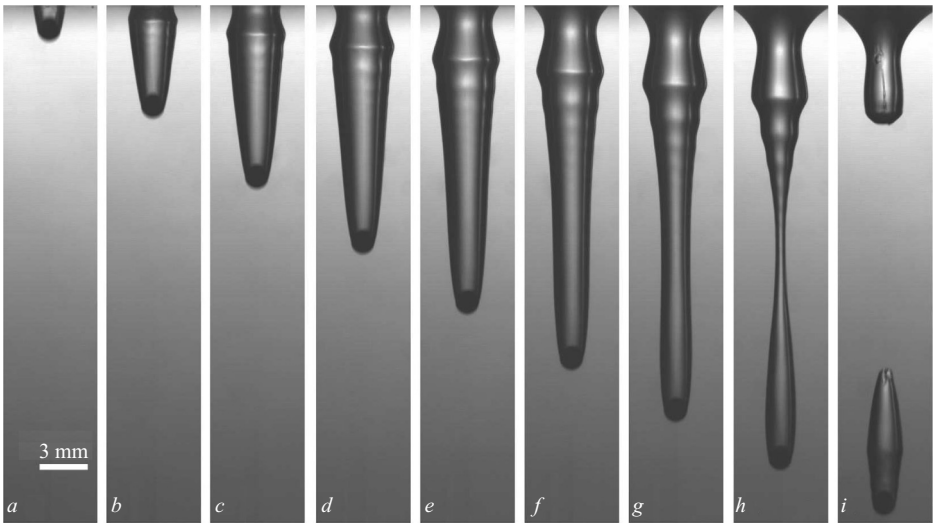

FIGURE 6. Deep seal impact cavity. Video sequence of the water entry of a hydrophobic steel sphere at low B ($R_0 = 0.079$ cm, $\rho_s = 7.7$ g cm^{-3}, $U_0 = 310$ cm s^{-1}). The time between successive images is 1.9 ms; $W = 109$; $B = 0.088$.

Deceleration of the sphere is minimal, and after descending 13 sphere diameters, the cavity first pinches at a depth of the order of the capillary length, entraining a volume of air much greater than that of the sphere. The entrained bubble may subsequently pinch off at depth, the likelihood of which is determined by the bubble size. This impact regime is characterized by its near-surface collapse and the presence of capillary waves and is henceforth referred to as 'shallow seal'.

Further increases in W give rise to a cavity of the form shown in figure 6. The impact is reminiscent of the shallow seal regime, generating a substantial air cavity and ripples that propagate down the resulting free surface. However, the pinch-off occurs at a greater depth, approximately halfway between the surface and the sphere. Moreover, the ripples are observed to propagate at speeds less than half of that of the sphere (see Appendix B), and thus do not appear to influence the pinch-off depth. This impact regime is henceforth referred to as 'deep seal'.

At the highest W considered, the cavity dynamics are as shown in figure 7. Here, the deep seal (figure 7*j*) is preceded by a closure event at the surface, known as 'surface seal' (figure 7*e*). The splash curtain created at impact domes over to seal the cavity from above, its collapse due to some combination of the curvature pressures $O(\sigma/R_0)$ and aerodynamic pressures $O\left(\rho_a U_0^2\right)$ acting on the splash curtain, the ratio of which is prescribed by $W\tilde{D}$. After the surface seal, the underlying cavity expands, and its pressure decreases, resulting in detachment from the surface (figure 7*f*). As the depth of water above the cavity increases, a Rayleigh–Taylor instability develops on the top of the cavity, and a water jet penetrates the cavity from above (figure 7*g*). This occurs when the hydrostatic pressure $\rho g z_c$, where z_c is the minimum cavity depth, surpasses the curvature pressure σ/R, i.e. when $\rho g R z_c/\sigma \gg 1$. In the underlying cavity, multiple pinch-offs may occur, with each successive pinch-off producing a bubble of decreasing volume.

A parameter study was conducted by varying the sphere size and release height, thus elucidating the influence of W and B on the water-entry cavity (see figure 8). At low B, the cavity type transitions from quasi-static to shallow seal to deep seal

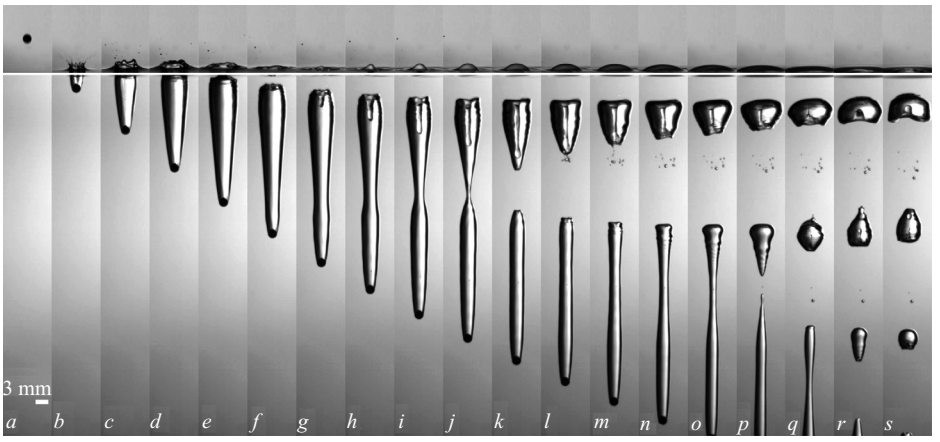

FIGURE 7. Surface seal impact cavity. Video sequence of the water entry of a hydrophobic steel sphere at low B ($R_0 = 0.10$ cm, $\rho_s = 7.7$ g cm^{-3}, $U_0 = 540$ cm s^{-1}). The time between successive images is 1.9 ms; $W = 420$; $B = 0.14$.

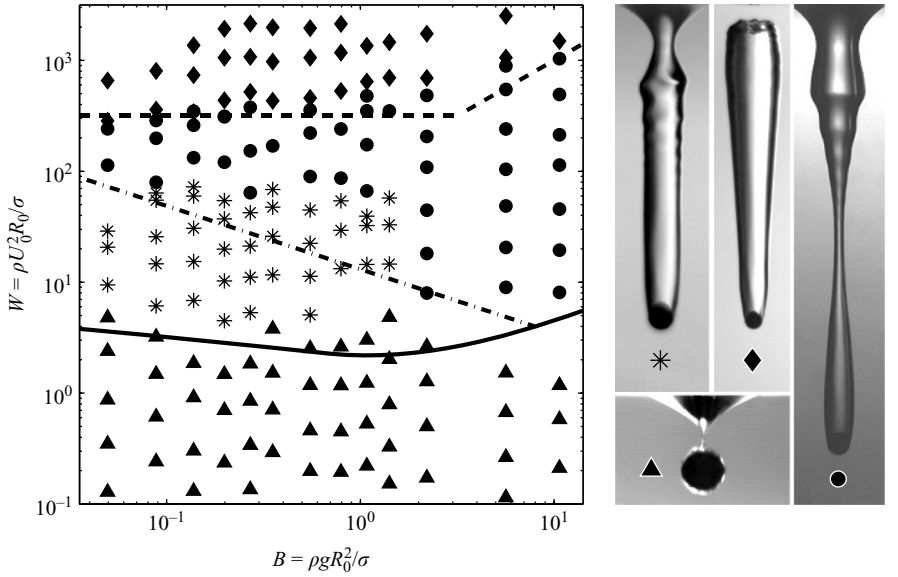

FIGURE 8. Regime diagram indicating the dependence of the observed cavity type on B and W for $\theta_a = 120°$. The triangle, asterisk, circle and diamond symbols denote the quasi-static, shallow seal, deep seal and surface seal regimes, respectively. The dash-dotted line is defined by (6.23*a*), and the solid curve by equating the pinch-off times defined by (5.5) and (6.3) for $\alpha = 0.065$ ($\theta_c = 166°$), $\theta_a = 120°$ and $C_a = 1/2$. The dashed line is given by the empirical fit $W = 320$ at low B (present study) and $F = (1/6\,400)\tilde{D}^{-2}$ at high B (Birkhoff & Isaacs 1951).

to finally surface seal as W is increased. The transition between the quasi-static and shallow seal regimes is slightly arbitrary but was taken as the W at which a volume of air comparable to that of the sphere is entrained by the sphere. The distinction between the shallow, deep and surface seal regimes was made on the basis of the pinch-off depth, z'_{pinch}: for $0 < z'_{pinch} < 2l_c$, the pinch-off was considered shallow, and

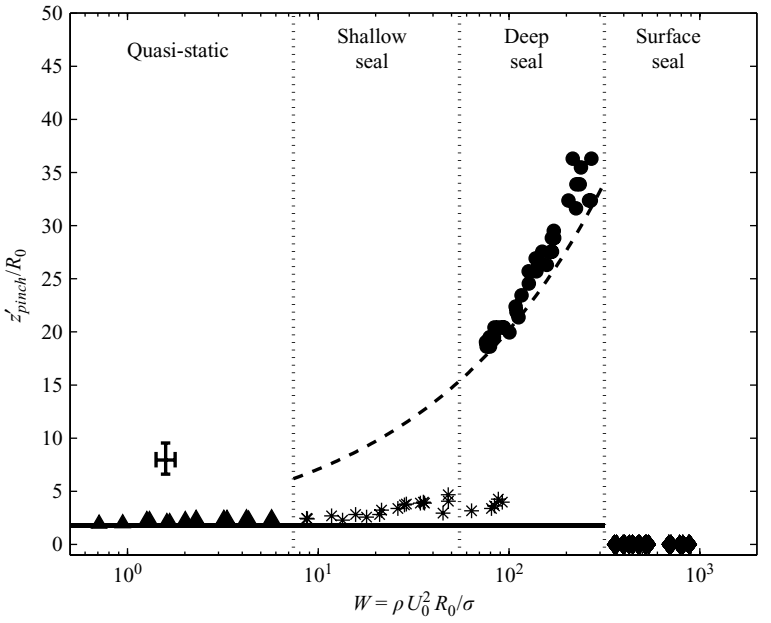

FIGURE 9. The dependence on W of the dimensionless pinch-off depth of the cavity generated by an impacting sphere for $B = \rho g R_0^2/\sigma = 0.088$, corresponding to $R_0 = 0.079$ cm and $\rho_s = 7.7\,\mathrm{g\,cm^{-3}}$. The cavity types quasi-static, shallow seal, deep seal and surface seal are denoted by the triangle, asterisk, circle and diamond symbols, respectively. The solid line denotes our theoretical prediction for the pinch-off depth of a quasi-static or shallow seal cavity and is given by (5.4*b*) for $\theta_a = 120°$. The dashed curve denotes our theoretical prediction for the pinch-off depth of a deep seal cavity, defined by (6.21*a*) with $\alpha = 0.065$ ($\theta_c = 166°$). Characteristic error bars are shown.

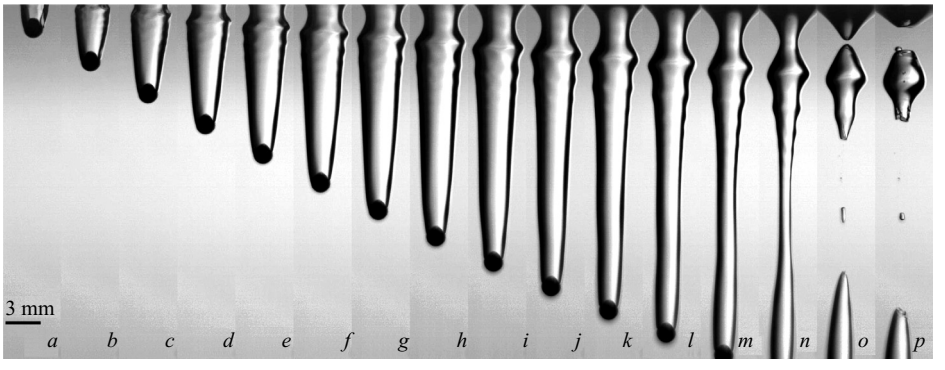

FIGURE 10. Video sequence of the water entry of a hydrophobic steel sphere, illustrating two nearly simultaneous pinch-off events ($R_0 = 0.079$ cm, $\rho_s = 7.7\ \mathrm{g\,cm^{-3}}$, $U_0 = 280\ \mathrm{cm\,s^{-1}}$). The time between successive images is 1 ms; $W = 88$; $B = 0.088$.

for $z'_{pinch} \geqslant 2l_c$, the pinch-off was considered deep. The theoretical curves demarcating the transitions between the regimes will be rationalized in § 6.

For a particular $B = 0.088$ ($R_0 = 0.079\,\mathrm{cm}$, $\rho_s = 7.7\,\mathrm{g\,cm^{-3}}$), the cavity evolution was studied in detail for $10^{-1} < W < 10^3$ and the pinch-off depth and time recorded. In figure 9, the observed W dependence of the pinch-off depth is shown. In the quasi-static regime, the pinch-off depth is approximately constant and equal to 75 % of

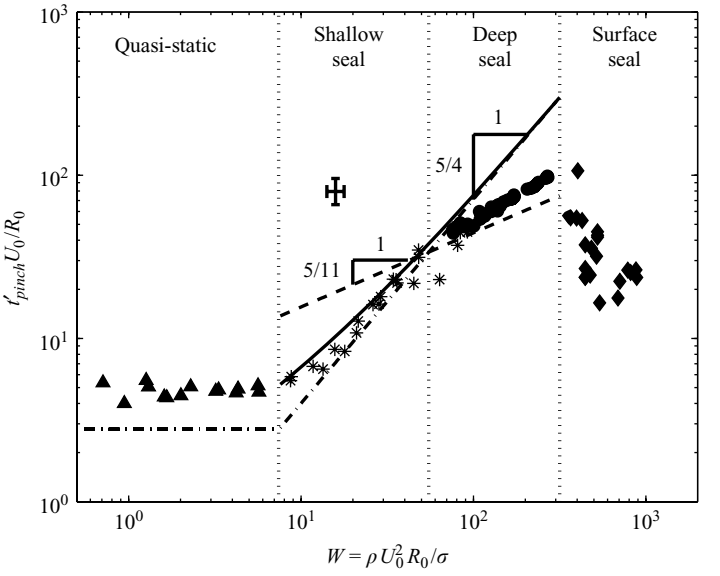

FIGURE 11. The dependence on W of the dimensionless pinch-off time of the cavity generated by an impacting sphere for $B = \rho g R_0^2/\sigma = 0.088$, corresponding to $R_0 = 0.079$ cm, and $\rho_s = 7.7$ g cm^{-3}. The cavity types quasi-static, shallow seal, deep seal and surface seal are denoted by the triangle, asterisk, circle and diamond symbols, respectively. The solid line denotes our theoretical prediction for the time of shallow seal, defined by (6.9) with $\alpha = 0.065$ ($\theta_c = 166°$). The dashed lines denote our theoretical prediction for the time of shallow seal and deep seal in the appropriate asymptotic limits, defined respectively by (6.10*a*) and (6.22*a*) with $\alpha = 0.065$ ($\theta_c = 166°$). The dash-dotted line denotes our theoretical prediction for the time of quasi-static pinch-off, defined by (5.5) with $\theta_a = 120°$. Characteristic error bars are shown.

the capillary length. In the shallow seal regime, a local maximum is achieved for $W = 35$. Gekle *et al.* (2008) observed analogous non-monotonic behaviour for $B = 50$ and attributed it to the capillary waves generated at impact that propagate down the cavity walls. In § 6.1, we will demonstrate that this explanation is also valid for low B impacts. Further increases in W result in the pinch-off depth increasing progressively until the surface seal regime is reached, upon which the pinch-off depth goes to zero. The abrupt increase in pinch-off depth observed between the shallow seal and deep seal regimes is exemplified in figure 10, where two nearly simultaneous pinch-off events are observed, one deep, the other shallow. In figure 11, the W dependence of the pinch-off time is shown. The pinch-off time is roughly independent of W for a given B in the quasi-static regime and then increases in the shallow seal and deep seal regimes, before finally decreasing in the surface seal regime. The observed W dependence of the pinch-off depths and times reported in figures 9 and 11 will be rationalized in §§ 5 and 6.

For $W \ll 1$, the dependence on B of the depth of the sphere's equator at which its cavity collapses (henceforth, the 'penetration depth') was recorded for $0.03 < B < 3$. This dependence is shown in figure 12 and will be rationalized in § 5. Impacts for $W \ll 1$ were obtained by attaching the spheres to rigid wires that were connected to a mechanical traverse. The spheres were then lowered into the water at speeds 0.4 cm s^{-1} $< U_0 <$ 1 cm s^{-1} to achieve impact Weber numbers in the range $10^{-4} < W < 10^{-2}$.

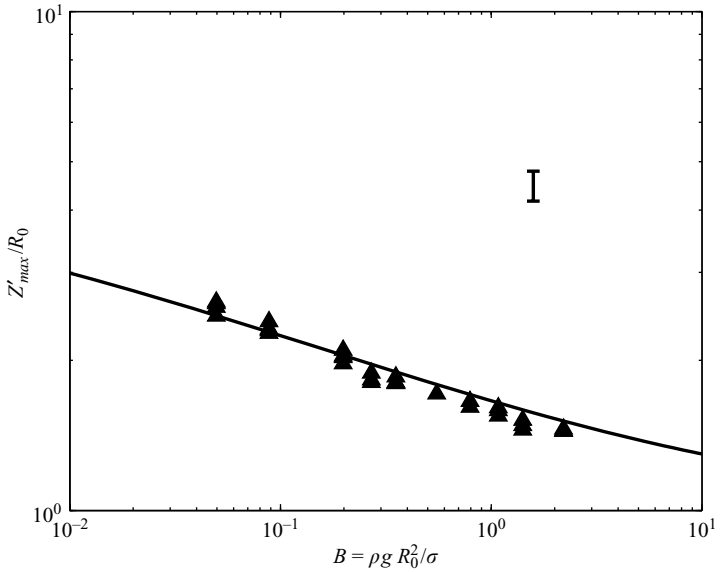

FIGURE 12. Penetration depth of a low speed ($W \ll 1$) impactor with a quasi-static cavity. The triangles denote the experimental data for impacting spheres ($10^{-4} < W < 10^{-2}$), and the solid curve is defined by (5.3) for $\theta_a = 120^\circ$, corresponding to the measured advancing contact angle. A characteristic error bar is shown.

3. Preliminary theoretical considerations

Following impact, the sphere sinks under the combined influence of gravity and its own inertia and is resisted by buoyancy, capillary and hydrodynamic forces. A vertical force balance on the sphere may be expressed as

$$(m + m_a)\ddot{Z}' = mg - F'_b - F'_c - F'_h, \tag{3.1}$$

where $Z'(t)$ is the mean depth of the sphere, the sphere's mass is $m = (4/3)\rho_s \pi R_0^3$, and primes denote dimensional quantities. $F'_b = \rho g \int\int_A z \, dA$ is the upward buoyant force due to hydrostatic pressure acting over the sphere's wetted surface area A. $F'_c = 2\pi R_0 \sigma \sin\beta \sin\psi$ is the upward force due to surface tension σ, where ψ is the angle the cavity adjoining the sphere makes with respect to the horizontal and $2\pi R_0 \sin\beta$ is the length of the contact ring (see figure 14). The vertical component of the total hydrodynamic force is given by $F'_h = -\int\int_A \hat{\boldsymbol{n}} \cdot \boldsymbol{T} \cdot \hat{\boldsymbol{z}} \, dA$, where $\boldsymbol{T} = -p_d \boldsymbol{I} + 2\eta \boldsymbol{E}$ is the stress tensor. We have separated the unsteady component of F'_h, the force required to accelerate the surrounding fluid, and expressed it in terms of an added mass, $m_a \approx C_m \rho R_0^3$, where C_m is the added mass coefficient. For a sphere moving in an unbound fluid, $C_m = 2/3$, which we take as the leading order estimate for the water entry of a sphere, while anticipating C_m to be a function of time (Miloh 1991). Substituting the dimensionless variables

$$Z = \frac{Z'}{R_0}, \quad t = t'\left(\frac{U_0}{R_0}\right) \tag{3.2}$$

and forces

$$F_c = \frac{F'_c}{R_0 \sigma}, \quad F_b = \frac{F'_b}{\rho g R_0^2 Z'}, \quad F_h = \frac{F'_h}{\rho R_0^2 U_0^2} \tag{3.3}$$

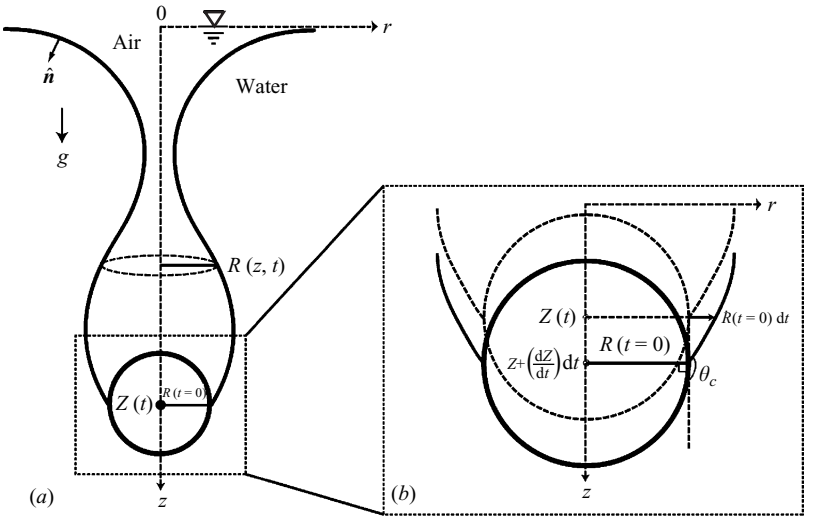

FIGURE 13. Sketch of (*a*) cavity model and (*b*) contact line model for shallow, deep and surface seal cavities. The cone angle, θ_c, is shown. A sketch of the contact line model for quasi-static cavities is illustrated in figure 14.

into (3.1) yields

$$\ddot{Z} = \left(\frac{D}{D+C_m}\right)\frac{B}{W} - \frac{BZ}{(D+C_m)W}F_b - \frac{1}{(D+C_m)W}F_c - \frac{Re-1}{(D+C_m)Re}F_h. \qquad (3.4)$$

Although F_b, F_c and F_h are not explicitly known, their magnitudes are $O(1)$, allowing us to simplify the description of the sphere's trajectory in various limits.

In our experimental study, $D \approx 7.7$, $B \ll 1$, $Re \gg 1$ and $10^{-1} < W < 10^3$. Thus, the gravitational, buoyancy and hydrodynamic forces given in (3.4) are negligible with respect to the curvature force, which gives rise to a characteristic dimensionless deceleration of the order $(WD)^{-1}$. For $WD \gg 1$, (3.4) further reduces to $\ddot{Z} = 0$, and although the sphere's speed may thus be treated as constant at the leading order in this limit, we will retain a term for the velocity of the sphere, $U(z)$, in our model, as it is straightforward to do so. We note that while the relevant parameter for determining the constancy of the sphere speed is WD, the relevant parameter for the cavity dynamics is W, as will be shown in §4. A study of the trajectory of an impacting sphere at low B was presented by Lee & Kim (2008). Here, we focus on the cavity dynamics for which the sphere trajectory simply provides a boundary condition for the evolution of the cavity.

4. Cavity dynamics: general formulation

The impact creates an axisymmetric air cavity that expands radially before closing under the combined influence of hydrostatic pressure, surface tension and aerodynamic pressure. A sketch of the cavity is shown in figure 13(*a*). We proceed by developing a general theoretical description of the cavity evolution and then examining the limits corresponding to the four observed cavity types: quasi-static, shallow seal, deep seal and surface seal. Particular attention is given to answering the question that motivated this study: at low B, when and where does the cavity collapse?

In the high Re limit, the motion of the liquid may be described at the leading order by the Euler equations:

$$\frac{\partial \boldsymbol{u}}{\partial t} + \boldsymbol{u}\cdot\nabla\boldsymbol{u} = -\frac{1}{\rho}\nabla p, \qquad \nabla\cdot\boldsymbol{u} = 0. \tag{4.1a, b}$$

Defining a velocity potential ϕ such that $\boldsymbol{u} = \nabla\phi$, we integrate (4.1$a$) to obtain the unsteady Bernoulli equation:

$$\left[\frac{\partial\phi}{\partial t} + \frac{u^2}{2} + \frac{p}{\rho} - gz\right]_A^B = 0, \tag{4.2}$$

where A and B represent any two points in the fluid. Choosing A to be at the interface and B to be far from the cavity but at the same depth gives

$$\left.\frac{\partial\phi}{\partial t}\right|_R + \left.\frac{u^2}{2}\right|_R = \frac{\sigma\nabla\cdot\hat{\boldsymbol{n}} + C_a\rho_a U_0^2 + \rho g z}{\rho}, \tag{4.3}$$

where $R(t, z)$ is the radius of the cavity. In (4.3), we have included the pressure jump across the interface due to surface tension $\sigma\nabla\cdot\hat{\boldsymbol{n}}$ and that due to air entering the cavity with characteristic speed U_0, where C_a is assumed to be a constant. This assumption is consistent with previous experiments that found that at high B, $7.5 < C_a < 10$, and no appreciable pressure gradients arose within the cavity over a range of impact speeds (Abelson 1970). In writing (4.3), we neglect any unsteadiness in the airflow, an assumption that is likely to be violated when the cavity becomes constricted near pinch-off. Next, we seek an appropriate potential ϕ that satisfies compressibility: $\nabla^2\phi = 0$.

Experiments conducted by Birkhoff & Caywood (1949) on water entry at high B and W have shown that the cavity motion is primarily radial or perpendicular to the cavity axis. We assume that this is likewise true at low B and so assume a purely radial motion $ru = R\dot{R}$, prescribed by that of the cavity walls having radial speed $\dot{R}(t, z)$. This approach thus yields a variant of the Rayleigh–Besant problem, the collapse of a spherical cavity (Rayleigh 1917; Besant 1859), and suggests a potential of the form

$$\phi = \begin{cases} R\dot{R}\ln\left(\dfrac{r}{R_\infty}\right) & \text{for } R < r < R_\infty, \\ 0 & \text{for } r > R_\infty, \end{cases} \tag{4.4}$$

where R_∞ is a function of time that ensures that the energy in a horizontal cross-section is finite, to be prescribed later. Duclaux *et al.* (2007) demonstrated the range of validity of cavity shapes predicted on the basis of (4.4) for high B impacts. Note that by choosing (4.4), we eliminate the axial fluid motion that typically accompanies the capillary instability of a vertical fluid cylinder, in particular, both travelling waves and classical Rayleigh–Plateau (Chandrasekhar 1961). Nevertheless, we shall demonstrate in § 6 that (4.4) provides an adequate description of the flow at low B, where the collapse is expected to be driven by surface tension.

Using (4.4), the total kinetic energy of a radially expanding fluid layer with thickness dz is

$$T = \frac{1}{2}\int_R^{R_\infty} 2\pi r\rho u^2 \mathrm{d}r\,\mathrm{d}z = \pi\rho\dot{R}^2R^2\ln(R_\infty/R)\mathrm{d}z. \tag{4.5}$$

Following Duclaux *et al.* (2007), we assume that $\ln(R_\infty/R) \approx 1$ and thus find that the radial fluid motion extends over a region comparable to the size of the cavity

($R_\infty \approx 2.7R$). Substituting (4.4) into (4.3) yields

$$R\ddot{R} + \frac{3}{2}\dot{R}^2 = -gz - \frac{\sigma}{\rho}(\nabla \cdot \hat{\boldsymbol{n}}) - C_a \frac{\rho_a}{\rho} U_0^2, \tag{4.6}$$

which is a form of the Rayleigh–Plesset equation with the addition of the hydrostatic and aerodynamic terms (Plesset & Prosperetti 1977). We proceed by non-dimensionalizing lengths by R_0 and time by R_0/U_0. In doing so, (4.6) becomes

$$W\left(R\ddot{R} + \frac{3}{2}\dot{R}^2\right) = -Bz - (\nabla \cdot \hat{\boldsymbol{n}}) - C_a \tilde{D} W. \tag{4.7}$$

To describe the time-dependent axisymmetric interface, we define the cavity surface $f(r, z, t) = r - R(z, t)$. The normal to the surface and its divergence are then

$$\hat{\boldsymbol{n}} = \frac{\nabla f}{|\nabla f|} = \frac{\hat{\boldsymbol{r}} - R_z \hat{\boldsymbol{z}}}{\left(1 + R_z^2\right)^{1/2}} \quad \text{and} \quad \nabla \cdot \hat{\boldsymbol{n}} = \frac{\left(1 + R_z^2\right)/R - R_{zz}}{\left(1 + R_z^2\right)^{3/2}}, \tag{4.8}$$

where $R_z = \partial R/\partial z$. We assume that the cavity walls have large slopes ($R_z \ll 1$) and that the longitudinal component of the curvature is negligible ($R_{zz} \ll 1$) to obtain

$$W\left(R\ddot{R} + \frac{3}{2}\dot{R}^2\right) = -Bz - \frac{1}{R} - C_a \tilde{D} W. \tag{4.9}$$

These assumptions provide a good description of the cavity sufficiently far from the surface ($z > l_c/R_0$), where the cavity is narrow and deep. There, we may consider the water entry problem in terms of independent horizontal fluid layers, each governed by (4.9).

The initial radial velocity of the cavity wall, $\dot{R}(t = 0)$, is related to the cone angle, θ_c, via a geometric argument illustrated in figure 13(*b*). Consider a contact line adjoining the sphere at depth Z. After an infinitesimal time $\mathrm{d}t$, the sphere descends a distance $(\mathrm{d}Z/\mathrm{d}t)\mathrm{d}t$, and the cavity expands by an amount $\dot{R}(t = 0)\mathrm{d}t$. Provided the contact line remains fixed with respect to the sphere, we find

$$\tan\left(\theta_c - \frac{\pi}{2}\right) = \frac{(\mathrm{d}Z/\mathrm{d}t)\mathrm{d}t}{\dot{R}(t = 0)\mathrm{d}t} = \frac{U(z)/U_0}{\dot{R}(t = 0)} = \frac{1}{\sqrt{\alpha}}, \tag{4.10}$$

where we have defined

$$\dot{R}(t = 0) = \sqrt{\alpha}\,\frac{U(z)}{U_0}. \tag{4.11}$$

Note that as $\alpha \to 0, \theta_c \to 180^\circ$. The assumption of the contact line remaining fixed near the sphere's equator was validated experimentally for the shallow, deep and surface seal regimes. Thus, we take $R(t = 0) = 1$.

At a given z, (4.9) may be integrated once in R to obtain

$$\dot{R}^2 = \left(\alpha \frac{U(z)^2}{U_0^2} + \frac{2Bz}{3W} + \frac{1}{W} + \frac{2}{3} C_a \tilde{D}\right) \frac{1}{R^3} - \frac{2Bz}{3W} - \frac{1}{WR} - \frac{2}{3} C_a \tilde{D}, \tag{4.12}$$

where we have used the initial condition (4.11). The maximum radius achieved by the cavity at a given depth, R^*, is found by setting (4.12) equal to zero and solving the resulting cubic to find

$$R^* = m + \sqrt[3]{q + \sqrt{q^2 - m^6}} + \sqrt[3]{q - \sqrt{q^2 - m^6}}, \tag{4.13}$$

where

$$m = -\frac{1}{2Bz + 2C_a \tilde{D} W} \tag{4.14}$$

and

$$q = m^3 - \frac{3m}{2}\left(\alpha W \frac{U(z)^2}{U_0^2} + 1\right) + \frac{1}{2}. \tag{4.15}$$

In the high W, high F, zero $\tilde{D}$ limit of (4.12), $\dot{R} = 0$ has no solution, and thus the cavity expands for all time and its radius evolves according to

$$R(t, z) = \left(\frac{5}{2} t \sqrt{\alpha} \frac{U(z)}{U_0} + 1\right)^{2/5} \sim t^{2/5} \tag{4.16}$$

as t goes to infinity. The time dependence of the cavity radius at a given depth is analogous to that of a blast wave generated by a nuclear explosion (Taylor 1950). Surface tension, gravity and air flow are negligible in this limit, and the cavity expansion is resisted only by the inertia of the fluid.

The cavity profile at time t^* is readily determined by integrating (4.12) from $z = 0$ to $z = Z(t^*)$, the dimensionless depth of the sphere's centre, and for each z from $t = 0$ to $t = t^* - t(z)$, the time elapsed since the sphere passed the depth z, with the initial condition $R(t = 0) = 1$. While (4.12) gives an expression for the cavity velocity, numerical integration is generally required to find the cavity evolution and pinch-off time. Nevertheless, in a few interesting limits, (4.12) may be integrated analytically.

5. Quasi-static impacts: $W \ll 1$

While the dynamics of cavity collapse is the thrust of our paper, we here briefly describe the quasi-static case, for which $W \ll 1$; (4.7) reduces to the Young–Laplace equation; and the cavity adjoining the object is in hydrostatic equilibrium. In this limit, the cavity shape, $R(z)$, is given by

$$Bz = -\nabla \cdot \hat{\boldsymbol{n}} = \frac{R_{zz} - \left(1 + R_z^2\right)/R}{\left(1 + R_z^2\right)^{3/2}} \tag{5.1}$$

with the boundary conditions

$$R_z(z = Z^*) = \cot\psi, \qquad R(z = 0) \to \infty, \tag{5.2a, b}$$

where $Z^* = Z + \cos\beta$ is the height of the contact line and $\psi = \theta_a + \beta - \pi$ as illustrated in figure 14. The time dependence enters only through the first boundary condition, rendering the problem quasi-static. We note that in the analogous planar problem, for the case of an infinitely long horizontal cylinder, it is possible to find a closed-form solution for the cavity shape (Ku, Ramsey & Clinton 1968). In the axisymmetric case, however, the boundary value problem given by (5.1) and (5.2a, b) must be solved numerically.

The penetration depth can now be understood as the maximum depth of the sphere's centre for which a solution to the boundary value problem exists. Let us denote this dimensionless depth as $Z_{max} = Z'_{max}/R_0$, where we use the prime symbol to signify dimensional quantities. In order to calculate Z_{max}, we use the following method: First, for a given B and θ_a, we pick a depth Z and search for a solution to (5.1) and (5.2a, b) over all possible positions of the contact ring (parameterized

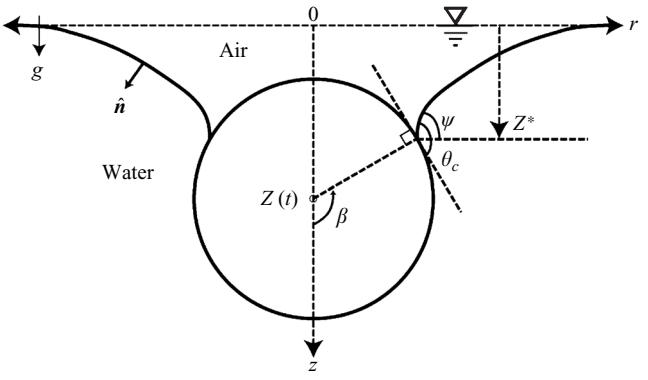

FIGURE 14. A hydrophobic sphere sinking through an air–water interface at $W \ll 1$. In this quasi-static limit, inertial effects are negligible, and the interface shape is prescribed by a static meniscus.

by β). If a solution exists, we increase Z and repeat the search. If no solution exists, we have found a depth for which a static meniscus cannot reach the sphere with the required contact angle. This method is repeated until the penetration depth is found.

Our results indicate that for $B \to 0$, the meniscus makes an angle $\psi \approx \theta_a/2$ with the horizontal when $Z = Z_{max}$. The maximum sphere density that an interface can support for $B \to 0$ is also attained when $\psi \approx \theta_a/2$ (Vella *et al.* 2006*a*) and thus provides validation of our numerical algorithm in this limit. On the other hand, we find that for $B \gg 1$, pinch-off takes place at the apex of the sphere, $\psi \approx \theta_a$, as one expects. Anticipating this asymptotic penetration depth dependence on the contact angle, the penetration depth data for $10^{-2} < B < 10^2$, shown in figure 15, is fit to the curve

$$Z'_{max}/R_0 \approx 0.83\, B^{-0.035 \log_{10} B - 0.31} \left(\sin \frac{\theta_a}{2}\right)^{1.6} + 1, \tag{5.3}$$

given by the solid curve in figure 15 (inset). Note that the maximum penetration depth occurs for $\theta_a = 180^\circ$ and that the penetration depth predicted by (5.3) does not scale with the capillary length, as would be the case for a sinking horizontal cylinder, where the meniscus is two-dimensional and $Z_{max} \sim B^{-1/2}$ (Vella *et al.* 2006*b*). In figure 12, we plot (5.3) for $\theta_a = 120^\circ$ as the solid curve along with the accompanying experimental data for $W \ll 1$. Satisfactory agreement is observed.

For $W \ll 1$, the pinch-off depth, z_{pinch}, and penetration depth satisfy the geometric relation

$$z_{pinch} = \begin{cases} Z_{max} - 1 & \text{for } B \gg 1, \\ Z_{max} + \cos\left(\pi - \frac{\theta_a}{2}\right) & \text{for } B \ll 1, \end{cases} \tag{5.4a, b}$$

where the numerically deduced dependence of ψ on the contact angle has been incorporated. Likewise, we can express the pinch-off time in terms of the pinch-off depth

$$t'_{pinch} \frac{U_0}{R_0} = \frac{z'_{pinch}}{R_0} + 1, \tag{5.5}$$

where we take $t = 0$ to correspond with $Z = 0$. The theoretically predicted pinch-off time (5.5) differs from that proposed by Lee & Kim (2008), who estimated the pinch-off time to be the time for a capillary–gravity wave to travel the capillary length, leading to $t_{pinch} \sim W^{1/2}$.

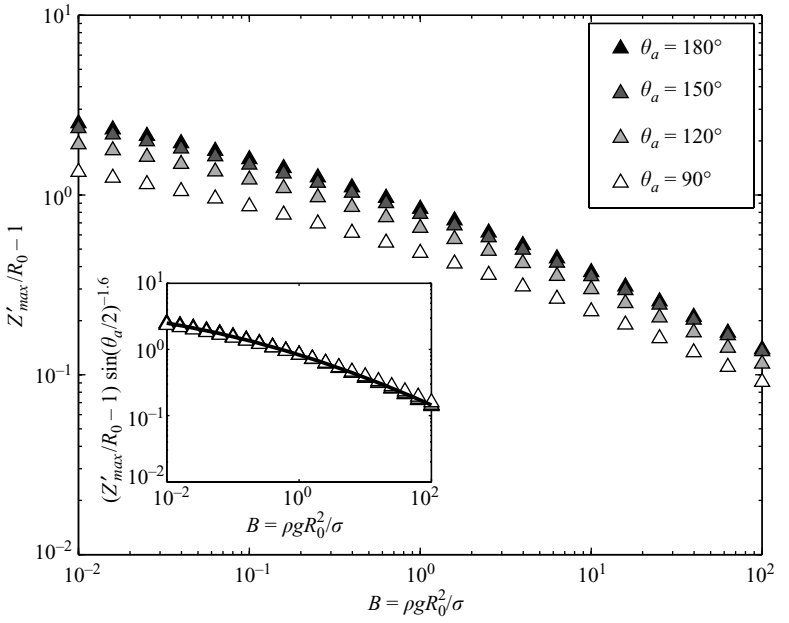

FIGURE 15. Penetration depth for a $W \ll 1$ impact. Theoretically predicted dependence of the dimensionless penetration depth on B for four values of the advancing contact angle, θ_a. Inset: data collapse showing that the solid curve, defined by (5.3), captures the dependence of the penetration depth on B and θ_a.

In figure 9, the pinch-off depth predicted by (5.4*b*) is given by the solid line, and in figure 11, the pinch-off time predicted by (5.5) is given by the dash-dotted line, in both cases for $B = 0.088$ and $\theta_a = 120°$. We note that inertia has been entirely neglected in the derivation of (5.5). For $W = O(1)$, the observed pinch-off time is greater than that given by (5.5), since dynamic effects, specifically the inertia of the radial outflow, presumably become significant and act to resist cavity collapse.

6. High speed impacts: $W > 1$

For $W > 1$, the inertial resistance to collapse must be included, but we may render the problem tractable by assuming $R_z \ll 1$ and $R_{zz} \ll 1$, as is appropriate for $z/l_c \gg 1$. The collapse time for a particular depth is found by integrating (4.12):

$$t_c(z) = \int_{R=1}^{R=R^*} G\left(R, W, Bz, C_a\tilde{D}, \alpha\frac{U^2}{U_0^2}\right) dR + \int_{R=0}^{R=R^*} G\left(R, W, Bz, C_a\tilde{D}, \alpha\frac{U^2}{U_0^2}\right) dR, \tag{6.1}$$

where

$$G = \left(\left(\alpha\frac{U(z)^2}{U_0^2} + \frac{2Bz}{3W} + \frac{1}{W} + \frac{2}{3}C_a\tilde{D}\right)\frac{1}{R^3} - \frac{2Bz}{3W} - \frac{1}{WR} - \frac{2}{3}C_a\tilde{D}\right)^{-1/2} \tag{6.2}$$

and R^* is defined by (4.13). The pinch-off time is the minimum time over depths $0 < z < \infty$ of the cavity collapse:

$$t_{pinch} = \min_{0<z<\infty}\left(t(z) + t_c(z)\right), \tag{6.3}$$

where $t(z)$ is the time taken for the sphere to arrive at depth z. We note that $t=0$ corresponds to $Z=0$, and z_{pinch} corresponds to the depth of fluid pinch-off. We proceed by seeking the pinch-off time and depth in the low and high B limits.

6.1. *Shallow seal*

For $Bz \ll 1$ and $1 < W \ll \tilde{D}^{-1}$, hydrostatic and aerodynamic pressures are negligible with respect to curvature pressures, and we expect pinch-off near the surface (see figure 5). This may be understood by considering the zero B limit of (4.12), which reduces to

$$\dot{R}^2 = \left(\alpha \frac{U(z)^2}{U_0^2} + \frac{1}{W}\right)\frac{1}{R^3} - \frac{1}{WR}. \tag{6.4}$$

According to (6.4), the evolution of the cavity depends on depth only through $U(z)$. For $|U_0 - U(z)|/U_0 \ll 1$, the speed of cavity collapse is depth-independent; therefore pinch-off occurs where the cavity was first initiated, at $z=0$, and at a time given by (6.3), which reduces to

$$t_{pinch} = \int_{R=1}^{R=R^*} \frac{\mathrm{d}R}{\sqrt{\left(\alpha + \frac{1}{W}\right)\frac{1}{R^3} - \frac{1}{WR}}} + \int_{R=0}^{R=R^*} \frac{\mathrm{d}R}{\sqrt{\left(\alpha + \frac{1}{W}\right)\frac{1}{R^3} - \frac{1}{WR}}}. \tag{6.5}$$

The maximum radial extent of the cavity (4.13) reduces to

$$R^* = \sqrt{\alpha W + 1}, \tag{6.6}$$

and by making the substitution $R = R^* \sin\vartheta$ and noting that $R^* \in [1, \infty)$, we reduce (6.5) to

$$t_{pinch} = R^{*3/2}\sqrt{W}\left(\int_{\vartheta^*}^{\pi/2} \sin^{3/2}\vartheta \,\mathrm{d}\vartheta + \int_0^{\pi/2} \sin^{3/2}\vartheta \,\mathrm{d}\vartheta\right), \tag{6.7}$$

where $\vartheta^* = \sin^{-1} R^{*-1}$. The integrals in (6.7) can be expressed in terms of the elliptic integral of the first kind,

$$J(\Phi, m) = \int_0^{\Phi} (1 - m\sin^2 x)^{-1/2}\mathrm{d}x, \tag{6.8}$$

to yield

$$\frac{3t_{pinch}}{R^{*3/2}W^{1/2}} = 2J\left(\frac{\pi - 2\theta^*}{4}, 2\right) + \sqrt{2}K\left(\frac{1}{2}\right) + 2\cos\theta^* \sin^{1/2}\theta^*, \tag{6.9}$$

where $K(m) = J(\pi/2, m)$. The asymptotic limits of (6.9) are found to be

$$t_{pinch} = \begin{cases} 2C_0\alpha^{3/4}W^{5/4} & \text{for } \alpha W \gg 1, \\ C_0\sqrt{W} & \text{for } \alpha W \ll 1, \end{cases} \tag{6.10a, b}$$

where

$$C_0 = \frac{\sqrt{2}}{3}K\left(\frac{1}{2}\right) \approx 0.874. \tag{6.11}$$

In figure 11, we plot the theoretically predicted pinch-off time (6.9) along with the asymptotic prediction (6.10*a*). The agreement between experiment and theory is good for $W < 100$, above which (6.9) and (6.10*a*) begin to overpredict the pinch-off time. Here, we no longer observe shallow seal cavities but instead observe that pinch-off occurs at greater depths (see figure 6), where hydrostatic pressure becomes

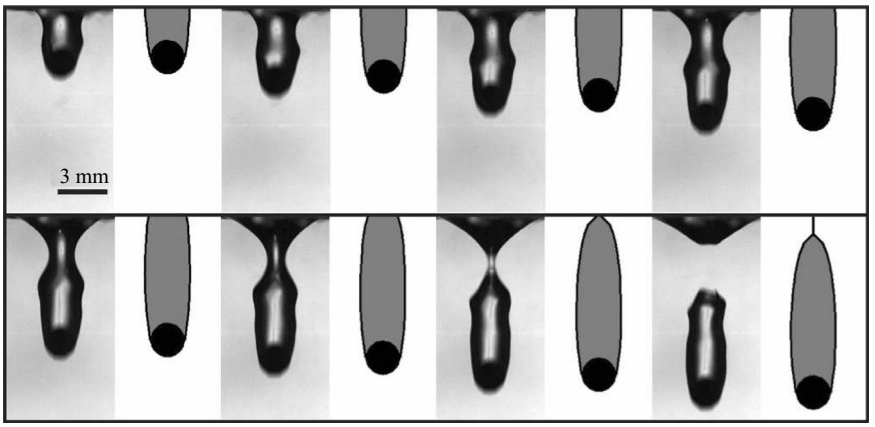

FIGURE 16. Zero B cavity model (6.4) alongside video sequence of shallow seal ($R_0 = 0.1$ cm, $\rho_s = 7.7$ g cm^{-3}, $U_0 = 110$ cm s^{-1}). The time between successive images is 1.1 ms; $W = 17$; $B = 0.14$ (experiment); $B = 0$ (model). Note that the model predicts pinch-off at the surface owing to the neglect of the longitudinal component of curvature.

increasingly important and accelerates pinch-off. The influence of hydrostatic pressure on the cavity evolution in this low B regime will be considered in § 6.2.

The theoretically predicted pinch-off time (6.10a, b) may also be understood by considering a simple balance between inertia and surface tension ($\rho U^2 \sim \sigma/a_0$), which leads to cavity collapse over a characteristic time scale

$$t'_{pinch} \sim \left(\frac{\rho a_0^3}{\sigma}\right)^{1/2}. \tag{6.12}$$

Note that the same scaling is obtained through consideration of the capillary instability of a hollow inviscid cylindrical jet in the absence of gravity, a variant of the classic Rayleigh–Plateau instability (Tomotika 1935; Chandrasekhar 1961). If we take a_0 to be the maximum radial extent of the cavity walls, $R_0 R^*$, where R^* is defined by (6.6), (6.12) may be expressed as

$$t'_{pinch}\frac{U_0}{R_0} \sim \begin{cases} \alpha^{3/4} W^{5/4} & \text{for } \alpha W \gg 1, \\ \sqrt{W} & \text{for } \alpha W \ll 1. \end{cases} \tag{6.13a, b}$$

We thus conclude that the theoretically predicted pinch-off time of a shallow seal cavity (6.10a, b) is consistent with its being a Rayleigh–Plateau-like instability, if one accounts for the initial expansion of the cavity walls as predicted by our theoretical model. The classic Rayleigh–Plateau pinch-off time, $t_{pinch} \sim \sqrt{W}$, is retained only when $\alpha W \ll 1$; i.e. the cavity walls do not expand. This limit is described further in Appendix A in the context of impacting vertical cylinders, for which the $\sqrt{W}$ scaling is indeed observed.

A comparison between the zero B model (6.4) and a particular shallow seal cavity is shown in figure 16, where we estimate $\theta_c = 168^\circ$ and prescribe the sphere trajectory from the video images. While the pinch-off time is predicted to be within 5 % of its observed value, we observe that shallow seal occurs not at the surface but at a depth of roughly the capillary length (see figures 5, 9 and 16). This discrepancy between experiment and theory may be attributed to the neglect of the longitudinal component of curvature in our theoretical model that resists collapse for $z < l_c$ and so tends to increase the pinch-off depth from $z'_{pinch} = 0$ to $z'_{pinch} \approx l_c$. Moreover, the

ripples observed on the cavity walls are not predicted by our theoretical model due to the use of a purely radial velocity potential, and hence do not appear in the model results shown in figure 16. For certain W ranges, we observe that the ripples reach the pinch-off depth at approximately the pinch-off time. The precise pinch-off depth is therefore influenced by the propagation of these waves, whose presence may account for the non-monotonic behaviour illustrated in figure 9. We note that the shallow seal regime is the most poorly described by our model, which neglects the longitudinal component of curvature that dominates the dynamics for $z/l_c \ll 1$.

The transition W from the quasi-static to shallow seal pinch-off may be estimated by equating the corresponding pinch-off times, (5.5) and (6.10a, b). In doing so, we find

$$W_1^* = \begin{cases} (2C_0)^{-4/5}\alpha^{-3/5}t_{pinch}^{4/5} & \text{for } \alpha W_1^* \gg 1, \\ C_0^{-2}t_{pinch}^2 & \text{for } \alpha W_1^* \ll 1. \end{cases} \tag{6.14a, b}$$

When $\alpha W_1^* = O(1)$, the pinch-off time given by (6.9) rather than (6.10a, b) should be used to estimate the transition W. We do so numerically for $\alpha = 0.065$ ($\theta_c = 166^\circ$) and $\theta_a = 120^\circ$, values appropriate for the impacting spheres used in our experiments, in order to deduce the solid curve in figure 8 for $B < 1$. The discrepancy may be attributed to the neglect of inertia in the derivation of (5.5), which resists collapse for $W > 1$ and would thus tend to increase both t_{pinch} and W_1^*.

6.2. *Deep seal*

The zero B model presented in § 6.1 predicts that pinch-off occurs at the surface $z = 0$. We expect this result to be flawed for two reasons. First, it neglects the longitudinal component of curvature that necessarily resists pinch-off at the surface. Second, hydrostatic pressure becomes important at depth, specifically, when $Bz \sim O(1)$. Thus, provided the W is sufficiently large so that the sphere reaches a dimensionless depth B^{-1} prior to pinch-off, hydrostatic pressure will be dynamically important during cavity collapse, and favour pinch-off at depth (see figure 9). We proceed by developing a description of deep seal pinch-off.

For $Bz \gg 1$ and $F \ll \tilde{D}^{-1}$, hydrostatic pressure dominates cavity collapse and (4.12) reduces to

$$\dot{R}^2 = \left(\alpha\frac{U(z)^2}{U_0^2} + \frac{2z}{3F}\right)\frac{1}{R^3} - \frac{2z}{3F}, \tag{6.15}$$

where we recall that $W = BF$. Provided that $|U_0 - U(z)|/U_0 \ll 1$, the collapse time, (6.1), reduces to

$$t_c(z) = \int_{R=1}^{R=R^*} \frac{\mathrm{d}R}{\sqrt{\left(\alpha + \frac{2z}{3F}\right)\frac{1}{R^3} - \frac{2z}{3F}}} + \int_{R=0}^{R=R^*} \frac{\mathrm{d}R}{\sqrt{\left(\alpha + \frac{2z}{3F}\right)\frac{1}{R^3} - \frac{2z}{3F}}}, \tag{6.16}$$

where

$$R^* = \sqrt[3]{\frac{3\alpha F}{2z} + 1}. \tag{6.17}$$

Substituting $R = R^* \sin^{2/3}\vartheta$ reduces (6.16) to

$$t_c(z) = R^*\sqrt{\frac{2F}{3z}}\left(\int_{\vartheta^*}^{\pi/2} \sin^{2/3}\vartheta\,\mathrm{d}\vartheta + \int_0^{\pi/2} \sin^{2/3}\vartheta\,\mathrm{d}\vartheta\right), \tag{6.18}$$

where $\vartheta^* = \sin^{-1} R^{*-3/2}$. For $\alpha F/z \ll 1$ ($R^* \to 1$, $\vartheta^* \to \pi/2$), the first integral in (6.18) vanishes, and for $\alpha F/z \gg 1$ ($R^* \to \infty$, $\vartheta^* \to 0$), the two integrals become equal. Thus,

(6.18) may be expressed as

$$t_c(z) = \begin{cases} 2C_1\alpha^{1/3}\left(\frac{3F}{2z}\right)^{5/6} & \text{for } \alpha F/z \gg 1, \\ C_1\left(\frac{3F}{2z}\right)^{1/2} & \text{for } \alpha F/z \ll 1, \end{cases} \tag{6.19a, b}$$

where C_1 may be expressed in terms of the gamma function:

$$C_1 = \frac{2\sqrt{\pi}\Gamma(11/6)}{5\Gamma(4/3)} \approx 0.747. \tag{6.20}$$

By solving (6.3) using (6.19a, b), we find the pinch-off depth

$$z_{pinch} = \begin{cases} C_2\alpha^{2/11}F^{5/11} & \text{for } \alpha F^{2/3} \gg 1, \\ C_3F^{1/3} & \text{for } \alpha F^{2/3} \ll 1, \end{cases} \tag{6.21a, b}$$

where $C_2 = (1/6)(3)^{10/11}(10C_1)^{6/11}$ and $C_3 = (1/2)(3C_1^2)^{1/3}$. Note that in our experiments, $5 < \alpha F^{2/3} < 15$ for $60 < W < 315$. In this W range, the theoretically predicted pinch-off depth (6.21a), represented by the dashed curve in figure 9, is in good agreement with experiment. This W range corresponds to the deep seal regime, where the cavity evolution is prescribed by (6.15), and it is safe to neglect surface tension. The pinch-off time, $t(z_{pinch}) + t_c(z_{pinch})$, is given by

$$t_{pinch} = \begin{cases} C_4\alpha^{2/11}F^{5/11} & \text{for } \alpha F^{2/3} \gg 1, \\ C_5F^{1/3} & \text{for } \alpha F^{2/3} \ll 1, \end{cases} \tag{6.22a, b}$$

where $C_4 = (11/5)C_2$ and $C_5 = 3C_3$. The theoretically predicted pinch-off time (6.22a), given by the dashed line in figure 11, is also in good agreement with experiment in this deep seal regime. We note that both (6.21a, b) and (6.22a, b) are compatible with the approximate analytical solutions and experimental observations of Duclaux *et al.* (2007), in which they propose $t_{pinch} \sim \alpha^{1/4}F^{1/2}$ for $\alpha F^{2/3} \gg 1$, and $t_{pinch} \sim F^{1/3}$ for $\alpha F^{2/3} \ll 1$.

The lower boundary of the deep seal regime, that is the W at which the cavity type transitions from shallow to deep seal, may be estimated by equating the shallow seal and deep seal pinch-off times, (6.10a, b) and (6.22a, b) respectively. Doing so yields the following transition W in various limits:

$$W_2^* = \begin{cases} \left(\dfrac{C_4}{2C_0}\right)^{44/35}\alpha^{-5/7}B^{-4/7} & \text{for } \alpha F^{2/3} \gg 1 \text{ and } \alpha W_2^* \gg 1, \\ \left(\dfrac{C_4}{C_0}\right)^{22}\alpha^4 B^{-10} & \text{for } \alpha F^{2/3} \gg 1 \text{ and } \alpha W_2^* \ll 1, \\ \left(\dfrac{C_5}{2C_0}\right)^{12/11}\alpha^{-9/11}B^{-4/11} & \text{for } \alpha F^{2/3} \ll 1 \text{ and } \alpha W_2^* \gg 1, \\ \left(\dfrac{C_5}{C_0}\right)^{6}B^{-2} & \text{for } \alpha F^{2/3} \ll 1 \text{ and } \alpha W_2^* \ll 1. \end{cases} \tag{6.23a–d}$$

We plot (6.23a) as the dash-dotted line in figure 8 for $\alpha = 0.065$, appropriate for our impacting spheres. The discrepancy for $B = O(1)$ likely arises from the admittedly arbitrary use of $2l_c$ as the cut-off depth used to distinguish between the deep and shallow seal regimes in our experiments.

In figure 17, we show a comparison between the theoretical model that includes both surface tension and hydrostatic pressure (4.12) and an experimentally observed deep

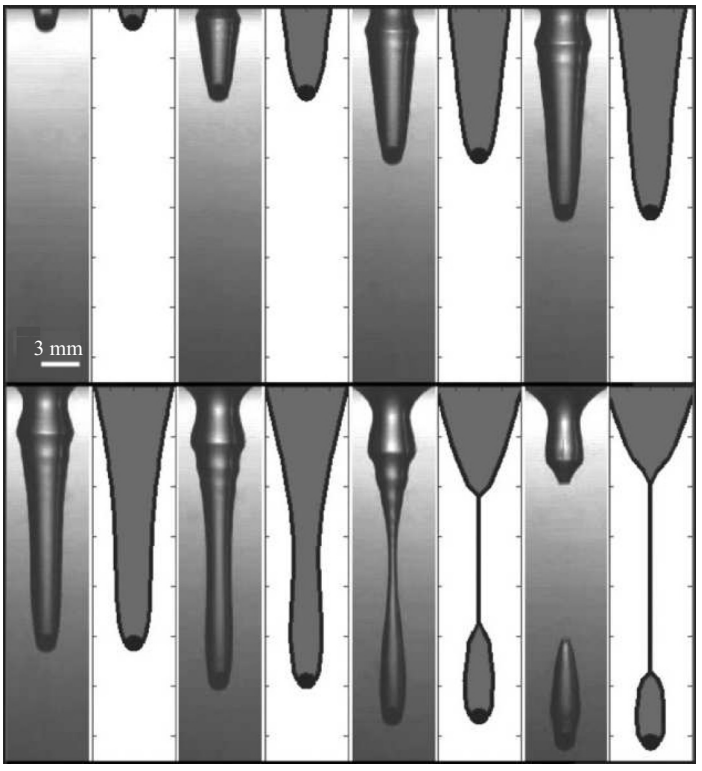

FIGURE 17. Cavity model (4.12) alongside video sequence of deep seal at low B ($R_0 = 0.08$ cm, $\rho_s = 7.7$ g cm^{-3}, $U_0 = 310$ cm s^{-1}). The time between successive images is 2.3 ms; $W = 109$; $B = 0.088$.

seal cavity, where we prescribe the sphere trajectory from video images and estimate $\theta_c = 160°$. The model captures the significant features of the cavity evolution, with the exception of the capillary waves and near-surface profile, shortcomings that result from neglecting vertical fluid motion and the longitudinal component of curvature. Despite the limitations of our theoretical model, the pinch-off time is predicted within 10 % of its observed value and the pinch-off depth to within 20 %.

For $B \gg 1$, one may estimate the transition from quasi-static to deep seal regimes by equating the corresponding pinch-off times (5.5) and (6.22a, b) to find

$$F_1^* = \begin{cases} C_6 \alpha^{-2/5} & \text{for } \alpha F_1^{*2/3} \gg 1, \\ C_7 & \text{for } \alpha F_1^{*2/3} \ll 1, \end{cases} \qquad (6.24a, b)$$

where $C_6 = C_4^{-11/5}$ and $C_7 = C_5^{-3}$. Note that the shallow seal regime does not exist for $B \gg 1$, nor does the deep seal regime exist for $B \ll 1$.

7. Surface seal

While the theoretical model developed in § 6 does not allow us to consider events above the surface, it does allow for consideration of the dependence of the cavity evolution on aerodynamic pressure. For $W \gg \tilde{D}^{-1}$ and $F \gg \tilde{D}^{-1}$, we may neglect curvature and hydrostatic pressures in favour of aerodynamic pressure. As described

in § 6.1, provided that $|U_0 - U(z)|/U_0 \ll 1$, pinch-off occurs where the cavity was first initiated, at $z = 0$. In this limit, (6.1) and (6.3) reduce to

$$t_{pinch} = \int_{R=1}^{R=R^*} \frac{\mathrm{d}R}{\sqrt{\left(\alpha + \frac{2}{3}C_a\tilde{D}\right)\frac{1}{R^3} - \frac{2}{3}C_a\tilde{D}}} + \int_{R=0}^{R=R^*} \frac{\mathrm{d}R}{\sqrt{\left(\alpha + \frac{2}{3}C_a\tilde{D}\right)\frac{1}{R^3} - \frac{2}{3}C_a\tilde{D}}}, \quad (7.25)$$

and (4.13) becomes

$$R^* = \sqrt[3]{3\alpha/(2C_a\tilde{D}) + 1}. \quad (7.26)$$

Substituting $R = R^* \sin^{2/3}\vartheta$ into (7.25) yields

$$t_{pinch} = R^* \sqrt{\frac{2}{3C_a\tilde{D}}} \left(\int_{\vartheta^*}^{\pi/2} \sin^{2/3}\vartheta \,\mathrm{d}\vartheta + \int_0^{\pi/2} \sin^{2/3}\vartheta \,\mathrm{d}\vartheta \right), \quad (7.27)$$

where $\vartheta^* = \sin^{-1} R^{*-3/2}$. Depending on the magnitude of $\alpha/\tilde{D}$, (7.27) reduces to the following:

$$t_{pinch} = \begin{cases} C_8\alpha^{1/3}(C_a\tilde{D})^{-5/6} & \text{for } \alpha/\tilde{D} \gg 1, \\ C_9(C_a\tilde{D})^{-1/2} & \text{for } \alpha/\tilde{D} \ll 1, \end{cases} \quad (7.4a, b)$$

where $C_8 = 2C_1(3/2)^{5/6}$, $C_9 = C_1(3/2)^{1/2}$ and C_1 is given by (6.20). We note that a simple balance between inertia and aerodynamic pressure $\left(\rho U^2 \sim \rho_a U_0^2\right)$ leads to the dimensionless pinch-off time scaling $t_{pinch} \sim \tilde{D}^{-1/2}$, which is retained when $\alpha/\tilde{D} \ll 1$ in (7.4*a*, *b*) and is in accord with a theoretical result obtained by Lee *et al.* (1997).

The theoretically predicted pinch-off time (7.4*a*, *b*) is found without considering the splash curtain dynamics; nevertheless, we expect it to set an upper bound for the time of surface seal. Moreover, we will demonstrate that our cavity model provides a good approximation of the initial conditions for the splash curtain. We proceed by considering the splash curtain dynamics.

For high B impacts, the time of surface seal is determined by the evolution of the splash curtain (Gilbarg & Anderson 1948; May 1952). At low B, we observe likewise (see figure 7) and so propose the following supplement to our cavity model: As illustrated in figure 18(*a*), we consider the splash curtain to be an axisymmetric liquid sheet with thickness $\delta(s)$ and speed $V(s)$, the evolution of which results in a closed bell shape (Clanet 2007). Provided that $F_s = V_0^2/(gH) \gg 1$, where H is the characteristic splash height, $H \approx R_0$ and V_0 the initial ejection speed, we can safely neglect gravity. Provided that air friction is negligible, one may further assume that $V(s) = V_0$. The evolution of the water bell is then described by a balance of inertia, surface tension and aerodynamic pressure. In dimensional variables, this balance takes the form

$$\left(W_s R'(t^*) - r'\right)\frac{\mathrm{d}\varphi}{\mathrm{d}s'} = -\cos\varphi - \frac{\triangle p}{2\sigma}r', \quad (7.5)$$

where $W_s = \rho V_0^2\delta_0/(2\sigma)$ is the Weber number of the sheet, s' the arc length along the sheet centreline and $\triangle p$ the pressure difference between the outside and inside of the bell (Clanet 2007). $R'(t^*)$ is the radial position at a time $t^* = t' - s'/V_0$ of the underlying cavity at $z' = 0$, which evolves according to (4.12) and so couples the dynamics of the cavity and splash curtain. Note that the existence of the splash curtain requires that $V_0 > V_c$, where $V_c = \sqrt{2\sigma/(\rho\delta)}$ is the retraction speed owing to surface tension (Taylor 1959; Culick 1960); thus, necessarily, $W_s > 1$.

The shape of the splash at time t' is obtained by integrating (7.5) from $s' = 0$ to $s' = V_0 t'$, with the initial conditions $r'(s' = 0) = R'(t', z' = 0)$ and

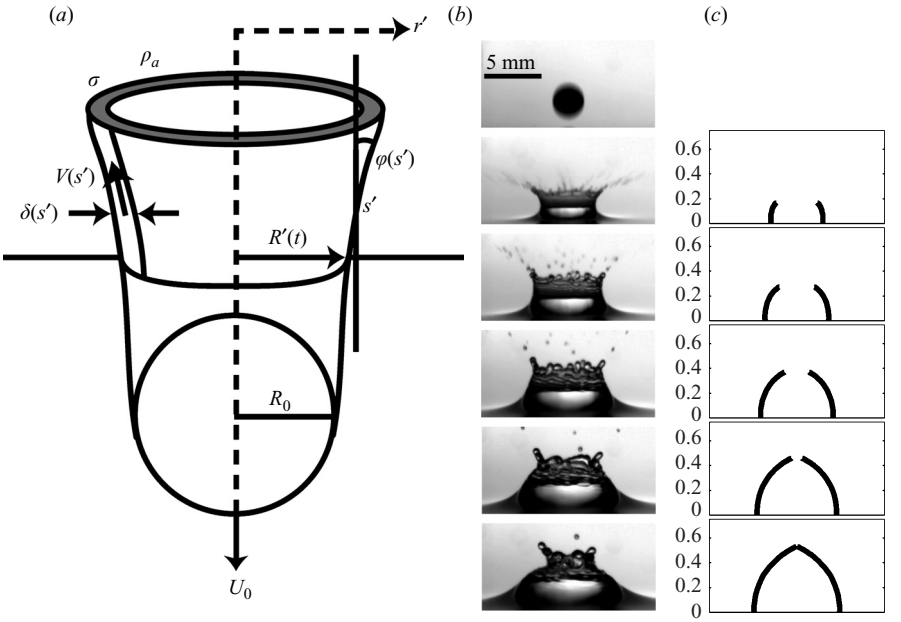

FIGURE 18. (*a*) Sketch of splash curtain model. (*b*) Video sequence of surface seal at $W = 570$, $B = 0.27$ ($R_0 = 0.14$ cm, $\rho_s = 7.7$ g cm^{-3}, $U_0 = 540$ cm s^{-1}). The time between successive images is 1 ms. (*c*) Predicted shape of splash curtain at times corresponding to experiment, where we measure $V_0/U_0 = 0.25 \pm 75\,\%$ and choose $\delta_0 = 0.02$ cm, corresponding to $W_s = 2.5$ and $F_s = 130$.

$\tan\varphi(s'=0) = \dot{R}'(t', z'=0)/U_0$, corresponding to the position and slope of the underlying cavity. Note that in writing (7.5), we assume that the initial sheet thickness δ_0 is independent of time. If one takes the characteristic pressure, length scale and time scale to respectively be $\rho_a U_0^2$, R_0 and R_0/V_0, (7.5) may be written in dimensionless form as

$$(W_s R(t-s) - r)\frac{\mathrm{d}\varphi}{\mathrm{d}s} = -\cos\varphi + \frac{W\tilde{D}}{2}r. \tag{7.6}$$

In the present study, $W \ll 2\tilde{D}^{-1} \approx 1\,700$; therefore, the collapse of the splash curtain is driven primarily by surface tension, and aerodynamic pressure may be safely neglected. Since the splash is axisymmetric, the initial sheet curvature draws the sheet inwards, resulting in a closed bell. The closure time of the splash curtain is obtained by considering the trajectory of the sheet's leading edge as prescribed by (7.6) for $t = s$, the time elapsed since impact, with the initial conditions $r(s=0) = 1$ and $\varphi(s=0) = \pi - \theta_c$. The solution is the catenary

$$\frac{r'}{R_0} = W_s - C_{10}\cosh\left(\frac{\frac{z'}{R_0} - C_{11}}{C_{10}}\right) \tag{7.7}$$

with integration constants

$$C_{10} = (1 - W_s)\cos\theta_c \quad \text{and} \quad C_{11} = C_{10}\ln\left(\frac{1+\sin\theta_c}{-\cos\theta_c}\right), \tag{7.8}$$

where the dependence on the cavity growth enters through the cone angle θ_c, the initial slope of the cavity wall defined by (4.11). Surface seal occurs when the sheet tip reaches zero radius, that is when $r' = 0$ in (7.7). Using the relation $s' = V_0 t'$, the

closure time is simply the arclength of (7.7) from $z=0$ to $r=0$:

$$t'_{closure}\frac{V_0}{R_0} = C_{10}\left[\sqrt{\left(\frac{W_s}{C_{10}}\right)^2 - 1} + \frac{\cos^2\theta_c - (\sin\theta_c + 1)^2}{2(\sin\theta_c + 1)\cos\theta_c}\right]. \tag{7.9}$$

A comparison between model (7.6) and experiment is made in figure 18(*b–c*). In the experiment, we measured $V_0/U_0 = 0.25 \pm 75\,\%$. While direct measurements of $\delta(s)$ were not possible, we used $\delta_0 = 0.02$ cm to initialize our simulations, which yielded a reasonable agreement. The dimensionless sheet thickness ($\delta_0/R_0 = 0.14$) is roughly consistent with those measured by Cossali *et al.* (2004), $0.1 < \delta(t')/R_0 < 1$, in an investigation of droplet impact on thin films for $140 < W < 430$. Using $\delta_0 = 0.02$ cm, we find $V_c = 85$ cm s^{-1}, which is small relative to $U_0 \sim 540$ cm s^{-1}; the difference between impact and sheet speeds thus cannot be rationalized wholly in terms of the rim retraction speed.

It is worth highlighting that the assumptions required to derive (4.12), including the neglect of the longitudinal component of curvature, are well satisfied in the surface seal regime. Specifically, since $\varphi_0 \approx 0$ in the experiments, (4.12) provides a good approximation for the radius and slope of the splash curtain at $z=0$. The principal shortcoming of our model for the splash curtain results from uncertainties in the sheet thickness and ejection speed, which may be influenced by sheet instability and droplet ejection (figure 18*b*). Nevertheless, our investigation has made clear that both the cavity and splash curtain need be considered to provide a full description of a surface seal cavity, and our model represents the first attempt to do so.

8. Discussion

We have presented the results of a combined theoretical and experimental investigation of the normal impact of hydrophobic bodies at low B, where the resulting cavity collapse is caused by both surface tension and gravity. This limit is relevant for the entry of small bodies ($R_0 \ll 2.7$ mm) into water. Our parameter study has revealed four distinct cavity types that arise as the W is progressively increased: quasi-static, shallow seal, deep seal and surface seal. In the quasi-static regime, the cavity takes the shape of a hydrostatic meniscus, and air entrainment is minimal. Both the shallow seal and deep seal regimes are characterized by considerable air entrainment, a long slender cavity and the occurrence of capillary waves but differ in terms of their pinch-off locations. In the surface seal regime, the splash created upon impact domes over to seal the cavity prior to its pinch off at depth.

A theoretical model based on the solution to the Rayleigh–Besant problem has been developed to describe the evolution of the cavity shape. The principal advantage of our model over full numerical simulations is its relative simplicity. It provides exact solutions for the evolution of the cavity and simple expressions for the pinch-off time and depth. Our theoretical developments also provide insight into the high B regime, where gravity is dominant with respect to surface tension. A summary of our new results for the cavity dynamics is given in table 2.

We have considered the influence of both curvature and aerodynamic pressures on the cavity evolution. The inclusion of surface tension allows us to describe low B impacts. Aerodynamic pressures become significant to the cavity dynamics when both $F\tilde{D} \gg 1$ and $W\tilde{D} \gg 1$. We may interpret the two distinct F scaling regimes observed by Gekle *et al.* (2008) for $B = 50$ as manifestations of the quasi-static and deep seal cavity types. We similarly observe a W regime in which the depth of pinch-off does

Limit	Result	Equation
$W \ll 1$	$Z_{max} \approx 0.83\, B^{-0.035 \log_{10} B - 0.31} \left(\sin \frac{\theta_a}{2}\right)^{1.6} + 1$	(5.3)
$B = 0,\ 1 < W \ll \tilde{D}^{-1},\ \alpha W \gg 1$	$t_{pinch} = 2C_0 \alpha^{3/4} W^{5/4}$	(6.10*a*)
$B = 0,\ 1 < W \ll \tilde{D}^{-1},\ \alpha W \ll 1$	$t_{pinch} = C_0 \sqrt{W}$	(6.10*b*)
$B \gg 1,\ 1 < F \ll \tilde{D}^{-1},\ \alpha F^{2/3} \gg 1$	$t_{pinch} = C_4 \alpha^{2/11} F^{5/11}$	(6.22*a*)
$B \gg 1,\ 1 < F \ll \tilde{D}^{-1},\ \alpha F^{2/3} \gg 1$	$z_{pinch} = C_2 \alpha^{2/11} F^{5/11}$	(6.21*a*)
$B \gg 1,\ 1 < F \ll \tilde{D}^{-1},\ \alpha F^{2/3} \ll 1$	$t_{pinch} = C_5 F^{1/3}$	(6.22*b*)
$B \gg 1,\ 1 < F \ll \tilde{D}^{-1},\ \alpha F^{2/3} \ll 1$	$z_{pinch} = C_3 F^{1/3}$	(6.21*b*)
$W \gg \tilde{D}^{-1},\ F \gg \tilde{D}^{-1},\ \alpha/\tilde{D} \gg 1$	$t_{pinch} \leqslant C_8 \alpha^{1/3} (C_a \tilde{D})^{-5/6}$	(7.4*a*)
$W \gg \tilde{D}^{-1},\ F \gg \tilde{D}^{-1},\ \alpha/\tilde{D} \ll 1$	$t_{pinch} \leqslant C_9 (C_a \tilde{D})^{-1/2}$	(7.4*b*)
$W \gg 1,\ F \gg 1,\ \tilde{D} = 0$	$R(t, z) = \left(\frac{5}{2} t \sqrt{\alpha (U(z)/U_0)} + 1\right)^{2/5}$	(4.16)

TABLE 2. Summary of cavity pinch-off results for the water entry of dense hydrophobic bodies, where t_{pinch} has been scaled by R_0/U_0, Z_{max} and z_{pinch} by R_0. Recall that $W = BF$.

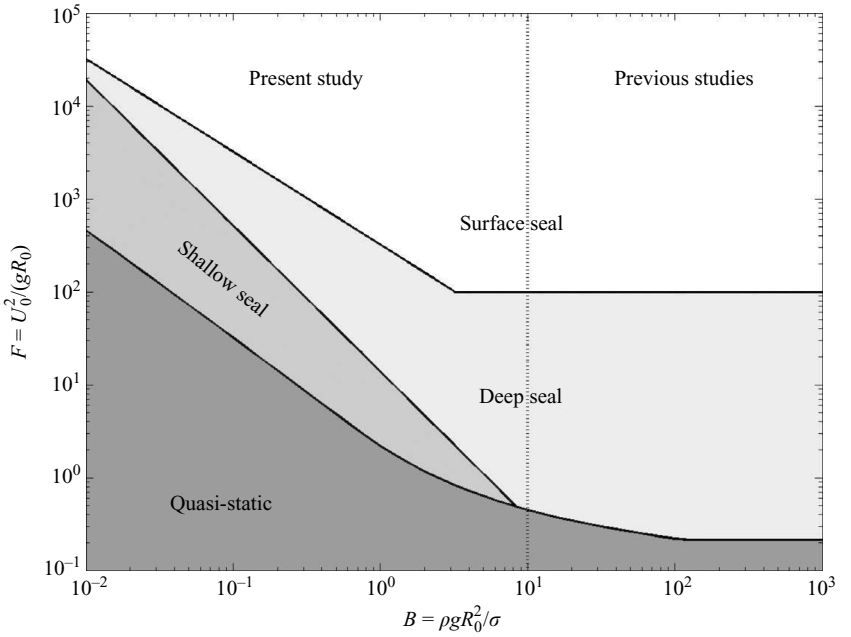

FIGURE 19. Regime diagram for the air–water entry of hydrophobic spheres, indicating the scope of the present study and observed cavity types (see § 2). For all studies, $Re \gg 1$, $D > 1$, $Q \gg 1$ and $\tilde{D} = 1.2 \times 10^{-3}$. The theoretically predicted boundaries between the cavity regimes are given in § 6, with the exception of the deep seal to surface seal boundary, given by the empirical fit $W = 320$ at low B (present study) and $F = (1/6\,400)\tilde{D}^{-2}$ at high B (Birkhoff & Isaacs 1951). Note that cavitation is expected to arise at sufficiently high speed – specifically, when $Q = (p - p_v)/(1/2\,\rho U_0^2) < 1$, where p_v is the liquid vapour pressure.

not increase monotonically. In figure 19, we thus present an expanded picture of the cavity dynamics of water entry, where the predicted cavity type depends on both F and B.

Our theoretical model captures the essential features of the water-entry cavity, as demonstrated by its ability to adequately predict the cavity shape, pinch-off time and

pinch-off depth. Our simplified description of the contact line dynamics provides a potential source of error, although the model does particularly well in the quasi-static, shallow seal and deep seal regimes. In the shallow seal and deep seal regimes, there are several possible sources of discrepancy between model predictions and experiment. First and foremost, the model neglects the longitudinal component of curvature, thus precluding adequate treatment of the near-surface region. Second, the model velocity field is purely radial, an assumption that is also likely to be violated in the near-surface region. Taken together, these assumptions preclude treatment of either the capillary waves propagating along the cavity walls or the classic Rayleigh–Plateau instability. Third, the two-dimensional geometry of the cavity obliged us to approximate the radial extent of the fluid motion generated by impact. The cavity model's ability to predict the time of surface seal is limited, as one expects the dynamics of the splash, which domes over to seal the cavity, to become important. Therefore, we have presented a supplemental model for the splash curtain dynamics that couples with our model of the cavity evolution. The splash is described as a water bell that evolves under the combined influence of surface tension, aerodynamic pressure and inertia. We thus obtain the dependence of the time of surface seal (7.9) on the sheet Weber number.

There are several outstanding questions that warrant further consideration, a number of which are currently under investigation. Lee & Kim (2008) consider sphere trajectories in the low B, low W regime and derive criteria for sphere rebound. We likewise intend to quantify the deceleration of impacting spheres at higher W. Second, while relatively high-speed, cavitating impacts have been examined experimentally by Shi, Itoh & Takami (2000) and Shi & Kume (2004), little has been done in terms of characterizing the influence of cavitation on the cavity shape. Finally, our study has made clear the important influence on the cavity dynamics of the wetting properties of the impactor. While the dependence of the cavity shape on the cone angle θ_c has been quantified, the precise relation between θ_c and θ_a has yet to be elucidated. A more detailed investigation of the wetting properties on both the cavity dynamics and impactor trajectory is ongoing.

The authors thank Christophe Clanet and Matthew Hancock for valuable discussions, Tadd Truscott and Daniel Hochbaum for their assistance with the experimental study and Alexandra Techet for access to her laboratory. J. W. M. B. gratefully acknowledges the financial support of the National Science Foundation through Grants CTS-0130465 and CTS-0624830, and J. M. A. of the National Defense Science and Engineering Graduate Fellowship Program.

Appendix A. Water entry of small hydrophobic cylinders

The cavity created in the wake of a vertical cylinder was examined in order to yield insight into the $\theta_c \to 180^\circ$ ($\alpha \to 0$) limit and, specifically, to test (6.10*b*). One expects to observe an earlier pinch-off time with respect to that of a sphere of equal values of W and B, because in this limit the cavity collapses without initially expanding. For a particular set of experiments, hydrophobic steel cylinders with radii $R_0 = 0.8$ mm were released from an electromagnet and the resulting cavity evolution recorded using high-speed video. The cylinders were sufficiently long (12 cm) so that the cavity formed following the initial entry of the cylinder had collapsed by the time the top of the cylinder entered the water. The cylinders were coated in the same manner as the spheres.

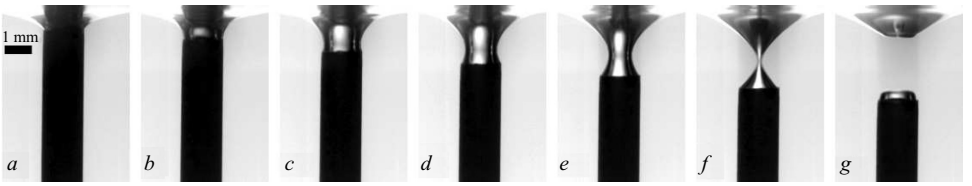

FIGURE 20. Quasi-static impact cavity. Video sequence of the top water entry of a steel cylinder at low B ($R_0 = 0.079$ cm, $\rho_s = 7.7$ g cm^{-3}, $U_0 = 60$ cm s^{-1}). The time between successive images is 1 ms; $W = 4$; $B = 0.088$.

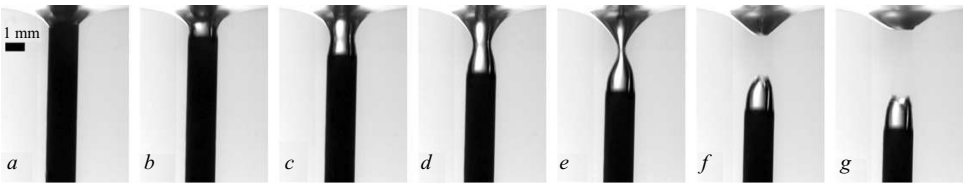

FIGURE 21. Shallow seal impact cavity. Video sequence of the top water entry of a steel cylinder at low B ($R_0 = 0.079$ cm, $\rho_s = 7.7$ g cm^{-3}, $U_0 = 141$ cm s^{-1}). The time between successive images is 0.7 ms; $W = 23$; $B = 0.088$.

For the impact of hydrophobic cylinders, we observed two distinct cavity types at low B according to W. A typical low W impact of a vertical cylinder is shown in figure 20. As the top edge of the cylinder enters the water, a transient air cavity is formed. The free surface attaches to the rim of the cylinder and is pulled downwards, taking the shape of a static meniscus. The radial extent of the cavity is comparable to the cylinder radius, and pinch-off occurs when the top of the cylinder reaches a depth on the order of the capillary length. Air entrainment is minimal. We denote this cavity type as 'quasi-static'.

As the W increases, a substantial air cavity is formed in the wake of the cylinder (see figure 21). Following water entry, the contact line becomes pinned to the cylinder's trailing edge, and the angle between the free surface and the vertical remains fixed at nearly 180°. The radial extent of the cavity is of the order of the cylinder's radius, and the top of the cylinder is deeper than the capillary length at pinch-off. The cavity pinches off at a depth of approximately the capillary length. The free surface is smooth, and we do not observe the generation of ripples. We denote this cavity type as 'shallow seal'.

For $W \ll 1$, we predict the pinch-off depth for the axisymmetric meniscus adjoining a cylinder by using a method similar to the one described in § 5. Let the cylinder have length $2l$ and radius R_0. As the cylinder sinks below the surface, the contact ring, located at depth Z^*, is pinned to the top edge of the cylinder, and ψ becomes independent of the contact angle. Thus, we have $Z^* = Z - l/R_0$ and allow ψ to take any value in the range $0 \leqslant \psi \leqslant \pi$. Given a depth Z of the cylinder, we search for a solution to (5.1) with the boundary conditions given by (5.2a, b). In this case, the maximum depth is achieved for $\psi \approx \pi/2$, and the pinch-off depth is given by

$$z'_{pinch}/R_0 \approx B^{-0.052 \log_{10} B - 0.35} \tag{A 1}$$

for $10^{-2} < B < 10^2$. Note the asymptotic behaviour in the limit of $\sigma = 0$ ($B \to \infty$): $z'_{pinch} \to 0$. In this limit, complete immersion takes place once the top edge of the cylinder reaches the surface.

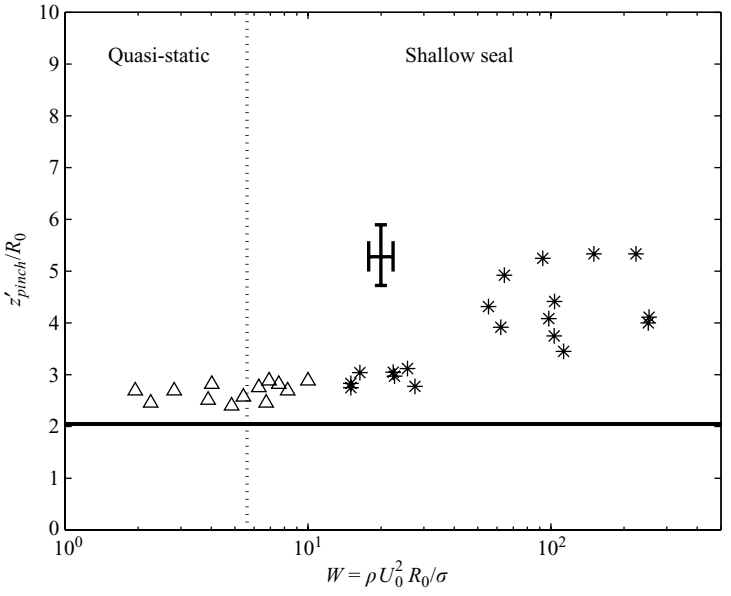

FIGURE 22. Dimensionless pinch-off depth of the cavity generated by an impacting vertical cylinder versus W for $B = \rho g R_0^2/\sigma = 0.088$, corresponding to $R_0 = 0.079$ cm. The cavity types quasi-static and shallow seal are denoted by the triangles and asterisks respectively. The solid line denotes our theoretical prediction for the pinch-off depth of a quasi-static or shallow seal cavity and is given by (A 1). Characteristic error bars are shown.

For $B = 0.088$, we present in figure 22 the experimentally observed pinch-off depths for the cavity created in the wake of a cylinder, along with the theoretically predicted pinch-off depth defined by (A 1). The small discrepancy in the quasi-static regime may be attributed to the neglect of inertia in the derivation of (A 1), which resists collapse for $W > 1$ and tends to increase z_{pinch}. The deviation between experiment and theory is expected to increase with increasing W. In figure 23, we present the experimentally observed pinch-off times, which are in reasonable agreement with our theoretical predictions; specifically (6.10*b*), given by the solid line and (A 1), given by the dash-dotted line. The neglect of inertia in the derivation of (A 1) leads to a discrepancy in the quasi-static regime. In the shallow seal regime, the neglect of the longitudinal component of curvature, which necessarily resists pinch-off, may account for the discrepancy. The study of impacting cylinders demonstrates that our theoretical model reasonably describes the cavity evolution in the limit $\alpha W \to 0$, where, according to (6.13*b*), the standard Rayleigh–Plateau pinch-off time $t_{pinch} \sim \sqrt{W}$ is obtained.

Appendix B. Cavity ripples

In § 2, we observed the presence of waves propagating along the vertical cavity walls (see figures 5 and 6). We here briefly examine the dynamics of these waves, which we propose may be understood by considering the stability of a hollow, inviscid cylindrical jet in the absence of gravity. Tomotika (1935) demonstrated that axisymmetric perturbations with wavelength λ less than the jet circumference $2\pi a_0$ are neutrally stable and propagate along the jet with the dispersion relation

$$\omega^2 = \frac{\sigma}{\rho a_0^3} \frac{\zeta K_1(\zeta)}{K_0(\zeta)} \left(\zeta^2 - 1\right), \quad \zeta = k a_0, \tag{B 1}$$

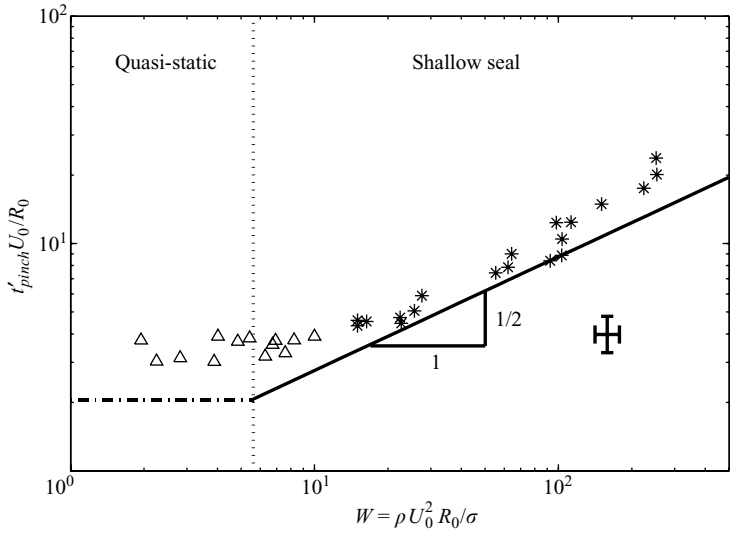

FIGURE 23. Dimensionless pinch-off time of the cavity generated by an impacting vertical cylinder versus W for $B = \rho g R_0^2/\sigma = 0.088$, corresponding to $R_0 = 0.079$ cm. The cavity types quasi-static and shallow seal are denoted by the triangles and asterisks respectively. The solid line denotes the theoretical pinch-off time of a shallow seal cavity and is given by (6.10*b*). The dash-dotted line denotes the theoretical pinch-off time of a quasi-static cavity, corresponding to (A 1) for $B = 0.088$. Characteristic error bars are shown.

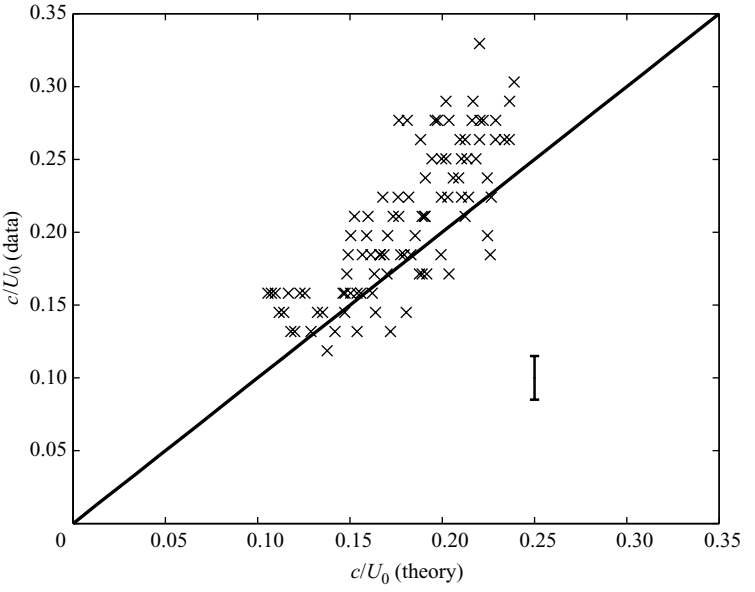

FIGURE 24. Analysis of ripples on a deep seal cavity for $W = 109$. Observed phase speed versus theoretical phase speed for the capillary waves supported by an inviscid cylindrical cavity in the absence of gravity. The theoretical phase speed is found by substituting the local values of a_0 and $k = 2\pi/\lambda$ into (B 1). A characteristic error bar is shown.

where K_0 and K_1 are modified Bessel functions of the second kind of orders zero and one respectively, a_0 is the radius, k is the wave vector, and ω is the frequency.

The initial disturbance is presumably associated with the large curvature at the surface, created by the sphere impact. Provided that the impact speed exceeds the capillary wave speed, that is $W > 1$, we may apply Tomotika's theory to the ripples on the water-entry cavity, noting that the condition $W > 1$ roughly coincides with the onset of the shallow seal regime. In our experiment, the Ohnesorge number $O = \eta^2/(\rho R_0 \sigma)$ is low ($10^{-6} < O < 10^{-4}$); so waves are not be greatly affected by viscosity. By tracking the positions of the wave crests for the deep seal impact shown in figure 6, we estimate the phase speed $c = \omega/k$ and dominant wavelength $\lambda = 2\pi/k$ for each crest. In figure 24, we compare the observed phase speed for a given k and local radius a_0 to the theoretically expected behaviour for capillary waves (B 1). The reasonable agreement suggests that the observed ripples are indeed capillary waves generated by the impacting body. Possible sources of error include the use of linear theory to describe the waves, as well as the neglected influence of the cavity motion on their propagation.

REFERENCES

Abelson, H. I. 1970 Pressure measurements in the water-entry cavity. *J. Fluid Mech.* **44**, 129–144.

Ablett, R. 1923 An investigation of the angle of contact between paraffin wax and water. *Philos. Mag.* **46**, 244–256.

Ashley, S. 2001 Warp drive underwater. *Sci. Amer.* **284**, 70–79.

Bell, G. E. 1924 On the impact of a solid sphere with a fluid surface. *Phil. Mag. J. Sci.* **48**, 753–765.

Bergmann, R., Meer, D., Stijnman, M., Sandtke, R., Prosperetti, A. & Lohse, D. 2006 Giant bubble pinch-off. *Phys. Rev. Lett.* **96** (154505), 1–4.

Besant, W. H. 1859 *Hydrostatics and Hydrodynamics*. Cambridge University Press.

Birkhoff, G. & Caywood, T. E. 1949 Fluid flow patterns. *J. Appl. Phys.* **20**, 646–659.

Birkhoff, G. & Isaacs, R. 1951 Transient cavities in air–water entry. *Tech. Rep.* 1490. Navord Rep.

Birkhoff, G. & Zarantonello, E. H. 1957 Jets, wakes and cavities. In *Applied Mathematics and Mechanics* (ed. F. N. Frenkiel), pp. 1–353. Academic.

Bush, J. W. M. & Hu, D. L. 2006 Walking on water: biolocomotion at the interface. *Annu. Rev. Fluid Mech.* **38**, 339–369.

Bush, J. W. M., Prakash, M. & Hu, D. L. 2008 The surface structure of water-walking arthropods: form and function. *Adv. Insect Physiol.* **34**, 117–192.

Chandrasekhar, S. 1961 *Hydrodynamic and Hydromagnetic Stability*. Dover.

Clanet, C. 2007 Waterbells and liquid sheets. *Annu. Rev. Fluid Mech.* **39**, 469–496.

Cossali, G. E., Marengo, M., Coghe, A. & Zhdanov, S. 2004 The role of time in single drop splash on thin film. *Exp. Fluids* **36**, 888–900.

Culick, F. E. C. 1960 Comments on a ruptured soap film. *J. Appl. Phys.* **31**, 1128.

De Gennes, P. G., Brochard-Wyart, F. & Quere, D. 2004 *Capillarity and Wetting Phenomena*. Springer.

Duclaux, V., Caillé, F., Duez, C., Ybert, C., Bocquet, L. & Clanet, C. 2007 Dynamics of transient cavities. *J. Fluid Mech.* **591**, 1–19.

Duez, C., Ybert, C., Clanet, C. & Bocquet, L. 2007 Making a splash with water repellency. *Nature Phys.* **3**, 180–183.

Gaudet, S. 1998 Numerical simulation of circular disks entering the free surface of a fluid. *Phys. Fluids* **10**, 2489–2499.

Gekle, S., van der Bos, A., Bergmann, R., van der Meer, D. & Lohse, D. 2008 Noncontinuous froude number scaling for the closure depth of a cylindrical cavity. *Phys. Rev. Lett.* **100**, 084502.

Gilbarg, D. & Anderson, R. 1948 Influence of atmospheric pressure on the phenomena accompanying the entry of spheres into water. *J. Appl. Phys.* **19**, 127–139.

Glasheen, J. W. & McMahon, T. A. 1996*a* A hydrodynamical model of locomotion in the basilisk lizard. *Nature* **380**, 340–342.

Glasheen, J. W. & McMahon, T. A. 1996*b* Vertical water entry of disks at low Froude numbers. *Phys. Fluids* **8**, 2078–2083.

Grumstrup, T., Keller, J. B. & Belmonte, A. 2007 Cavity ripples observed during the impact of solid objects into liquids. *Phys. Rev. Lett.* **99** (114502), 1–4.

Hiemenz, P. C. & Rajagopalan, R. 1997 *Principles of colloid and surface chemistry*. CRC Press.

Howison, S. D., Ockendon, J. R. & Wilson, S. K. 1991 Incompressible water-entry problems at small deadrise angles. *J. Fluid Mech.* **222**, 215–230.

Korobkin, A. A. & Pukhnachov, V. V. 1988 Initial stage of water impact. *Annu. Rev. Fluid Mech.* **20**, 159–185.

Kralchevsky, P. A. & Denkov, N. D. 2001 Capillary forces and structuring in layers of colloid particles. *Curr. Opin. Coll. Interf. Sci.* **6**, 383–401.

Ku, T. C., Ramsey, J. H. & Clinton, W. C. 1968 Calculation of liquid droplet profiles from closed-form solution of young-laplace equation. *IBM J. Res. Develop.* **12**, 441–447.

Lee, D. G. & Kim, H. Y. 2008 Impact of a superhydrophobic sphere onto water. *Langmuir* **24**, 142–145.

Lee, M., Longoria, R. G. & Wilson, D. E. 1997 Cavity dynamics in high-speed water entry. *Phys. Fluids* **9**, 540–550.

Lohse, D., Bergmann, R., Mikkelsen, R., Zeilstra, C., van der Meer, D. M., Versluis, M., van der Weele, K., van der Hoef, M. & Kuipers, H. 2004*a* Impact on soft sand: void collapse and jet formation. *Phys. Rev. Lett.* **93**, 198003, 1–4.

Lohse, D., Rauhe, R., Bergmann, R. & van der Meer, D. 2004*b* Granular physics: creating a dry variety of quicksand. *Nature* **432**, 689–690.

Mallock, A. 1918 Sounds produced by drops falling on water. *Proc. R. Soc. Lond.* A **95**, 138–143.

Mansfield, E. H., Sepangi, H. R. & Eastwood, E. A. 1997 Equilibrium and mutual attraction or repulsion of objects supported by surface tension. *Phil. Trans. R. Soc. Lond.*A **355**, 869–919.

May, A. 1951 Effect of surface condition of a sphere on its water-entry cavity. *J. Appl. Phys.* **22**, 1219–1222.

May, A. 1952 Vertical entry of missiles into water. *J. Appl. Phys.* **23**, 1362–1372.

May, A. 1975 Water entry and the cavity-running behavior of missiles. *Tech Rep.* 20910. Naval Surface Weapons Center White Oak Laboratory.

Melosh, H. J. 1980 Cratering mechanics – observational, experimental, and theoretical. *Annu. Rev. Earth Planet. Sci.* **8**, 65–93.

Melosh, H. J. & Ivanov, B. A. 1999 Impact crater collapse. *Annu. Rev. Earth Planet. Sci.* **27**, 385–415.

Miloh, T. 1991 On the initial-stage slamming of a rigid sphere in a vertical water entry. *Appl. Ocean Res.* **13**, 43–48.

Oliver, J. M. 2007 Second-order wagner theory for two-dimensional water-entry problems at small deadrise angles. *J. Fluid Mech.* **572**, 59–85.

Plesset, M. S. & Prosperetti, A. 1977 Bubble dynamics and cavitation. *Annu. Rev. Fluid Mech.* **9**, 145–185.

Rayleigh, LORD 1917 On the pressure developed in a liquid during the collapse of a spherical cavity. *Phil. Mag.* **34**, 94–98.

Richardson, E. G. 1948 The impact of a solid on a liquid surface. *Proc. Phys. Soc.* **61**, 352–367.

Shi, H. H., Itoh, M. & Takami, T. 2000 Optical observation of the supercavitation induced by high-speed water entry. *Trans. ASME* **122**, 806–810.

Shi, H. H. & Kume, M. 2004 Underwater acoustics and cavitating flow of water entry. *Acta Mechanica Sinica* **20**, 374–382.

Taylor, G. I. 1950 The formation of a blast wave by a very intense explosion. *Proc. R. Soc. Lond.* A **201**, 159–186.

Taylor, G. I. 1959 The dynamics of thin sheets of fluid: waves on fluid sheets. *Proc. R. Soc. Lond.* A **253**, 296–312.

Thoroddsen, S. T., Etoh, T. G., Takehara, K. & Takano, Y. 2004 Impact jetting by a solid sphere. *J. Fluid Mech.* **499**, 139–148.

Thoroddsen, S. T. & Shen, A. Q. 2001 Granular jets. *Phys. Fluids* **13**, 4–6.

Tomotika, S. 1935 On the instability of a cylindrical thread of a viscous liquid surrounded by another viscous fluid. *Proc. R. Soc. Lond.* A **150**, 322–337.

Vella, D., Lee, D. G. & Kim, H. Y. 2006*a* The load supported by small floating objects. *Langmuir* **22**, 5979–5981.

Vella, D., Lee, D. G. & Kim, H. Y. 2006*b* Sinking of a horizontal cylinder. *Langmuir* **22**, 2972–2974.

Vella, D. & Metcalfe, P. 2007 Surface tension dominated impact. *Phys. Fluids* **19**, 072108.

Von Karman, T. 1929 The impact on seaplane floats during landing. *Tech Rep.* 321. NACA.

Wagner, H. 1932 Phenomena associated with impacts and sliding on liquid surfaces. *ZAMM* **12**, 193–235.

Ward, J. V. 1992 *Aquatic Insect Ecology: Biology, and Habitat*. John Wiley.

Whalley, I. A. 2002 Project upkeep – a review of the WWII dambuster weapon. In *Proc. 38th AIAA/ASME/SAE/ASEE Joint Propulsion Conf. Exhibit*. American Institute of Aeronautics and Astronautics Inc., Indianapolis, IN.

Worthington, A. M. & Cole, R. S. 1897 Impact with a liquid surface, studied by the aid of instantaneous photography. *Phil. Trans. R. Soc. Lond.* A **189**, 137–148.

Worthington, A. M. & Cole, R. S. 1900 Impact with a liquid surface, studied by the aid of instantaneous photography: paper 2. *Phil. Trans. R. Soc. Lond.* A **194**, 175–199.